J. Fluid Mech. (2007), *vol.* 570, *pp.* 177–215.
doi:10.1017/S0022112006002941 Printed in the United Kingdom

Two-dimensional simulation of unsteady heat transfer from a circular cylinder in crossflow

By SALEM BOUHAIRIE AND VINCENT H. CHU

Department of Civil Engineering and Applied Mechanics, McGill University, Montreal, Québec, H3A 2K6, Canada

(Received 10 July 2005 and in revised form 15 June 2006)

The heat transfer from the surface of a circular cylinder into a crossflow has been computed using a two-dimensional model, for a range of Reynolds numbers from $Re = 200$ to 15 550. The boundary-layer separation, the local and overall heat-transfer rates, the eddy- and flare-detachment frequencies and the width of the flares were determined from the numerical simulations. In this range of Reynolds numbers, the heat-transfer process is unsteady and is characterized by a viscous length scale that is inversely proportional to the square root of the Reynolds number. To ensure uniform numerical accuracy for all Reynolds numbers, the dimensions of the computational mesh were selected in proportion to this viscous length scale. The small scales were resolved by at least three nodes within the boundary layers. The frequency of the heat flares increases, and the width of each flare decreases, with the Reynolds number, in proportion to the viscous time and length scales. Despite the presence of three-dimensional structures for the range of Reynolds numbers considered, the two-dimensional model captures the unsteady processes and produced results that were consistent with the available experimental data. It correctly simulated the overall, the front-stagnation and the back-to-total heat-transfer rates.

1. Introduction

The release of thermal energy from a heated circular cylinder into a crossflow is a problem of advection and diffusion that depends on the Reynolds and Prandtl numbers. At high Reynolds numbers, the thermal energy is trapped in the thin boundary layers on both the front and back surfaces of the cylinder. The subsequent release of thermal energy is through the separation of the boundary layers from the back surface and the formation of narrow pathways directed away from the cylinder wall. The challenge in numerical solution of the problem is to resolve the steep thermal and velocity gradients on the surface of the cylinder and, at the same time, to calculate the heat transfer through the narrow pathways with equal accuracy. Past heat-transfer calculations of the flow around a circular cylinder were conducted typically up to a Reynolds number of 200 (Dennis, Hudson & Smith 1968; Sunden 1983; Patnaik, Narayana & Seetharamu 1999; Hatanaka & Kawahara 1995; Karniadakis 1988; Lange, Durst & Breuer 1998). Recent calculations have been pushed to a Reynolds number as high as 3900 (Xia & Karniadakis 1997). There have not been any significant attempts to calculate the heat-transfer rate at higher Reynolds numbers. However, the velocity field around the circular cylinder has been calculated at significantly higher Reynolds numbers (see table 1). Highly accurate numerical calculations for the velocity have been conducted using the streamfunction and vorticity formulation

Authors	*Re*	Setup	Results
heat-transfer calculations			
Wood (1968)	0.3	2D full	ψ, ω, T, Nu
Dennis *et al.* (1968)	$0.01 \sim 40$	2D half	ψ, ω, T, Nu
Sunden (1983)	$5 \sim 40$	2D half	ψ, ω, T, Nu
Karniadakis (1988)	$20 \sim 200$	2D full	$T(t), Nu_s, Nu(\theta), \overline{Nu}$
Hatanaka & Kawahara (1995)	100	2D full	$u, v, p, T, St(Ri)$
Patnaik *et al.* (1996)	200	2D full	u, v, p, T, Nu, St
Lange *et al.* (1998)	$10^{-4} \sim 200$	2D full	u, v, p, T, Nu
Xia & Karniadakis (1997)	500, 3900	3D full	$u, v, w, p, \omega, T, Nu$
Pinol & Grau (1998)	60, 100, 200	2D full	$\psi, \omega, C_D, C_L, St, Nu$
Patnaik *et al.* (1999)	20–40	2D full	$u, v, p, T, St(Ri), Nu(Ri)$
Nakamura & Kamemoto (2001)	200–1000	2D full	ω, T, Nu
flow calculations			
Thom (1933)	10, 20	2D half	ψ, ω, C_p
Payne (1958)	40, 100	2D half	ω, C_D
Kawaguti & Jain (1966)	$1 \sim 100$	2D half	ψ, ω, C_p, C_D
Son & Hanratty (1969)	40, 200, 500	2D half	ψ, ω, C_D
Dennis & Chang (1969)	40	2D half	ψ, ω, C_p, C_D
Jain & Rao (1969)	40, 60, 100, 200	2D half	ψ, ω, C_p, C_D
Thoman & Szewczyk (1969)	$1 \sim 3 \times 10^5$	2D full	ψ, ω, C_D, St
Dennis & Chang (1970)	$5 \sim 100$	2D half	ψ, ω, C_D
Dennis & Staniforth (1971)	100, 500, 1000, 10 000	2D half	ψ, ω, C_D
Jordan & Fromm (1972)	100, 400, 1000	2D full	$\psi, \omega, C_D, \theta_s$
Collins & Dennis (1973*a*)	100, 200	2D half	$\psi, \omega, C_D, \theta_s$
Collins & Dennis (1973*b*)	$1 \sim \infty$	2D half	$\psi, \omega, C_p, \theta_s$
Patel (1976)	$60 \sim 600$	2D half	$\psi, \omega, C_D, \theta_s$
Ta Phuoc Loc (1980)	300, 550, 1000	2D half	ψ, ω, C_D
Ta Phuoc Loc & Bouard (1985)	$3000 \sim 9500$	2D half	ψ, ω
Braza *et al.* (1986)	100, 200, 1000	2D full	u, v, p, θ_s
Smith & Stansby (1988)	$250 \sim 10^5$	2D half	$\psi, \omega, C_D, \theta_s$
Sa & Chang (1990)	20, 100	2D half	ψ, ω, C_D, St
Song & Yuan (1990)	$1.4 \times 10^5 \sim 8.4 \times 10^6$	2D full	u, v, p, C_D
Engelman & Jamnia (1990)	100	2D full	u, v, p, C_D
Tezduyar & Liou (1991)	100	2D full	ψ, ω, C_D
Behr *et al.* (1991)	100	2D full	ψ, ω, C_D
Karniadakis & Triantafyllou (1992)	$200 \sim 500$	3D full	u, v, w, p, St
Behr *et al.* (1995)	100	2D full	u, v, p
Mittal (1996)	3900, 5000	3D full	u, v, w, p, C_p, C_D, St
Nair & Sengupta (1996)	10 000	2D full	ψ, ω, C_D
Jordan & Ragab (1998)	5600	3D full LES	$u, v, w, p, C_p, C_D, \theta_s, \nu_{sgs}$
Persillon & Braza (1998)	$100 \sim 300$	3D full DNS	u, v, w, p
Zhang & Dalton (1998)	200	3D full	u, v, w, p, C_D, C_L, St
Mittal (2001)	1000	3D full	u, v, w, p, C_D, C_L, St
Singh & Mittal (2003)	$10^5 \sim 10^6$	2D full	$u, v, p, C_D, C_L, k, E(k)$
Singh & Mittal (2004)	$100 \sim 10^7$	2D full	$u, v, p, k, E(k)$

TABLE 1. Numerical calculations of heat transfer and flow around a circular cylinder. 2D, two-dimensional simulation; 3D, three-dimensional simulation; half, half-cylinder; full, full cylinder; LES, large eddy simulation; DNS, direct numerical simulation.

by Daube & Ta Phouc Loc (1978) and by Ta Phouc Loc & Bouard (1985), for flow past a half-circular cylinder at Reynolds numbers as high as 9500. Large-eddy simulation (LES) using a three-dimensional LES model was conducted by Jordan & Ragab (1998) for $Re = 5600$. Karniadakis & Triantafyllou (1992), Persillon & Braza (1998) and Mittal (2001) have conducted direct numerical simulation (DNS) of the turbulent flow in the wake of the circular cylinder, up to a Reynolds number of 1000. More recently, Dong & Karniadakis (2005) performed three-dimensional DNS for drag and lift coefficients up to a Reynolds number as high as $Re = 10\,000$.

Since the heat-transfer rate is proportional to the temperature gradients, the computation grid must be sufficiently refined to resolve these steep gradients on the surface of the cylinder. The higher the Reynolds number, the finer is the requirement for the computation grid. The success of the simulation also depends on the implementation of the boundary conditions. In this study, the size of the grid was selected to be proportional to the boundary-layer thickness. Therefore, the grid becomes more refined with increasing Reynolds number. The wall vorticity was calculated using a compact finite-difference scheme to the third order of accuracy. The simulations of the heat-transfer process were conducted for Reynolds numbers $Re = 200$, 1000, 5000, 8290 and 15 550, with Prandtl number $Pr = 0.7$. The local and overall heat-transfer rates, the back-to-total heat-transfer ratios, the angles of flow separations and the eddy- and flare-detachment frequencies were determined from the simulations.

Most laboratory heat-transfer studies in the past have been concerned with the overall heat-transfer coefficient and its correlations with the Reynolds and Prandtl numbers (Hilpert 1933; Eckert & Soehngen 1952; Dimopoulos & Hanratty 1968; Eckert & Drake 1972; Zukauskas & Ziugzda 1986). However, Eckert & Soehngen (1952), Schmidt & Wenner (1943), Krall & Eckert (1973) and Adachi, Okamoto & Adachi (1979) were able to obtain the circumferential distribution of the local coefficient from their measurements. A comprehensive state-of-the-art review is given in the two-volume book by Zdrakovich (1997, 2003). The measurements by Schmidt & Wenner (1943) were most significant, covering a wide range of Reynolds numbers from $Re = 5000$ to 426 000. They found that the back–side heat-transfer rate increased continuously with Reynolds number. At high Reynolds numbers, the heat-transfer rate on the back surface was observed to be higher than the rate at the front. As it will be shown from the two-dimensional calculations presented in this paper, their observation is related to the formation of thermal layers on the back surface. The thermal layers are unsteady, unlike the boundary layer developing from the front. However, they play the same role in keeping the thermal energy close to the wall. Despite the onset of three-dimensionality in this range of Reynolds numbers, the two-dimensional model on a fine grid was able to confirm and provide explanation of the high back–side heat-transfer rate. Without a doubt, there is some disparity between the two-dimensional and three-dimensional simulation results. For example, the fluctuating lift is one parameter that is incorrectly predicted by the two-dimensional model (Norberg 2003; Dong & Karniadakis 2005). Nevertheless, many other thermal and flow parameters are closely approximated by the two-dimensional model. The objective of the present numerical simulation was to provide a complete set of highly consistent two-dimensional results, rather than to compare the two-dimensional and three-dimensional models. In this way, the validity and limitation of the two-dimensional model can be judged fairly in the future, when three-dimensional results of comparable accuracy become available for comparison in the same range of Reynolds numbers.

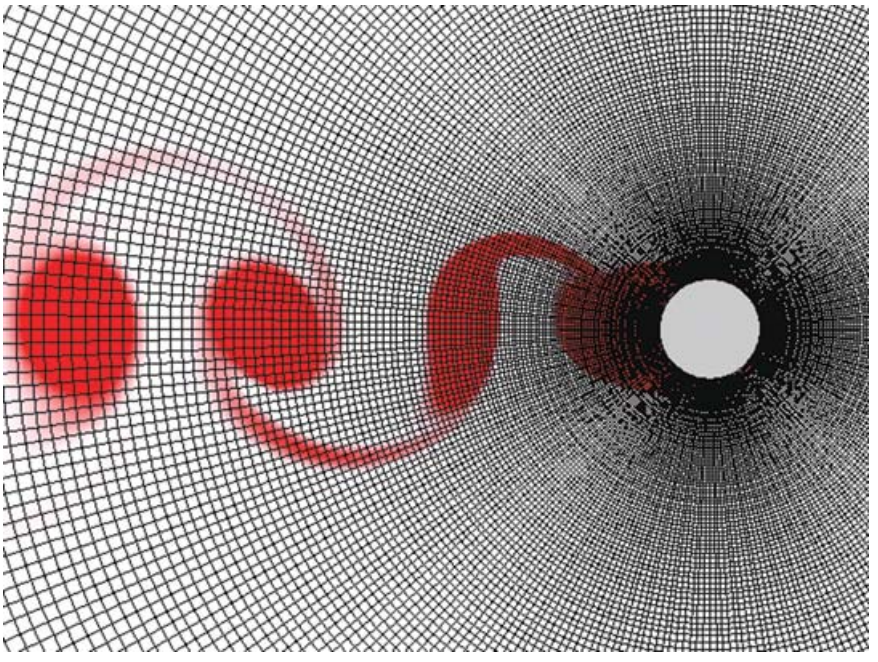

FIGURE 1. Wake behind a heated circular cylinder at dimensionless time $t = 70$ for Reynolds number $Re = 1000$. The flow approaches the cylinder from the right to the left in the figure. The computational grid in cylindrical coordinates is shown as an overlay.

2. Formulation

The numerical computations were conducted for two-dimensional incompressible flow using a streamfunction and vorticity formulation. The calculations were carried out using transformed coordinates. The relationships between the transformed coordinates ξ, η and the polar coordinates r, θ are

$$r = a\,\mathrm{e}^{\pi\xi}, \qquad \theta = \pi\eta. \tag{2.1}$$

A uniform grid in the transformed coordinates corresponds to a non-uniform grid in the physical coordinates, as shown in figure 1. A fine grid in the vicinity of the cylinder ensures accurate calculations of the gradients on the surface of cylinder, which are necessary for prediction of the boundary-layer separation and the heat flux from the surface of the cylinder.

In the transformed coordinates, the vorticity ω is related to the streamfunction ψ through the Poisson equation

$$\frac{\partial^2\psi}{\partial\xi^2} + \frac{\partial^2\psi}{\partial\eta^2} = g\omega, \tag{2.2}$$

where $g = \pi^2\,\mathrm{e}^{2\pi\xi}$ is the Jacobian of the transformation. The velocity components in the transformed coordinates are

$$V = -\frac{\partial\psi}{\partial\eta}, \qquad U = \frac{\partial\psi}{\partial\xi}. \tag{2.3}$$

Re	D (m)	$\tilde{T}_{wall}$ (°C)	$\tilde{T}_{\infty}$ (°C)	U_{∞} (m s^{-1})	Pr	Pe	I_m	J_m
200	0.0254	74.0	24.0	0.12	0.71	142	70	140
1000	0.0350	74.0	24.0	0.44	0.71	710	150	300
5000	0.0500	100.0	24.0	1.54	0.71	3550	340	680
8290	0.0500	100.0	24.0	2.55	0.71	5886	430	860
15 550	0.1000	100.0	24.0	2.40	0.71	11 040	600	1200

TABLE 2. Parameter values and conditions for the numerical simulations.

The advection–diffusion equations for the vorticity ω and the temperature T in the transformed coordinates are

$$g\frac{\partial\omega}{\partial t}+\frac{\partial(\omega U)}{\partial\eta}+\frac{\partial(\omega V)}{\partial\xi}=\frac{\partial}{\partial\xi}\left(\frac{2}{Re}\frac{\partial\omega}{\partial\xi}\right)+\frac{\partial}{\partial\eta}\left(\frac{2}{Re}\frac{\partial\omega}{\partial\eta}\right), \tag{2.4}$$

$$g\frac{\partial T}{\partial t}+\frac{\partial(TU)}{\partial\eta}+\frac{\partial(TV)}{\partial\xi}=\frac{\partial}{\partial\xi}\left(\frac{2}{Pe}\frac{\partial T}{\partial\xi}\right)+\frac{\partial}{\partial\eta}\left(\frac{2}{Pe}\frac{\partial T}{\partial\eta}\right), \tag{2.5}$$

where T is the temperature excess relative to the ambient temperature. The Reynolds number $Re=U_{\infty}D/\nu$ and the Peclet number $Pe=U_{\infty}D/\alpha$ are defined in terms of the diameter of the cylinder D and the upstream velocity U_{∞}. However, the dimensionless time $t=U_{\infty}\tilde{t}/a$, the dimensionless vorticity $\omega=\tilde{\omega}a/U_{\infty}$ and the dimensionless streamfunction $\psi=\tilde{\psi}/(U_{\infty}a)$ are based on the radius of the cylinder a.

The numerical solution of the Poisson equation was obtained using a Hermitian scheme. Daube & Ta Phouc Loc (1978) used this scheme to calculate the flow around an impulse-started half-cylinder and obtained a vorticity distribution in near perfect agreement with the laboratory observations by Coutanceau & Bouard (1979) and Coutanceau & Defaye (1991). They reproduced the observed details of the secondary-eddy and forewake phenomena. Their computations, however, were limited to the flow past a half-cylinder over a very short period of time after an impulsive start and did not include heat-transfer results. The present computation extended the application of this numerical scheme to heat-transfer calculations for a full cylinder at higher Reynolds numbers.

Table 2 summarizes the conditions of the present numerical simulations. The fluid around the cylinder is air, for which the molecular viscosity and thermal diffusivity are temperature dependent. The temperature on the surface of the cylinder, T_{wall}, is uniform. Its values are given in the table. The conditions of these numerical simulations were selected so that the results could be compared with the local heat-transfer measurements on the surface of the cylinder for Reynolds numbers $Re=8290$ and 15 550 by Schmidt & Wenner (1943). In Schmidt & Wenner's experiments, the surface temperature of a hollow brass cylinder was kept constant at 100 °C by the condensation of water vapour on the inner surface of the cylinder, except for a narrow instrumentation strip that was heated separately to nearly the same temperature by electricity. The heat flux by radiation was deducted from their measurements. Although the simulations are for an incompressible fluid, the density, viscosity and heat conductivity are treated in the simulation as variable and temperature dependent. The incompressible assumption is acceptable for the moderate range of Mach numbers varying from $Ma=0.0001$ to 0.04 in the present series of numerical simulations. Buoyancy is also ignored in the numerical results presented in this paper. The effect

of buoyancy is found to be negligible by comparing the results obtained between simulations that were conducted with and without it.

3. Compact difference scheme

The Poisson equation for the streamfunction, (2.2), is solved numerically by a compact-difference scheme, which treats the zeroth, first and second derivatives of the streamfunction as independent variables:

$$\psi_{i,j}^{n}, \qquad \left(\frac{\partial\psi}{\partial\xi}\right)_{i,j}^{n}, \qquad \left(\frac{\partial\psi}{\partial\eta}\right)_{i,j}^{n}, \qquad \left(\frac{\partial^2\psi}{\partial\xi^2}\right)_{i,j}^{n}, \qquad \left(\frac{\partial^2\psi}{\partial\eta^2}\right)_{i,j}^{n}. \tag{3.1}$$

These independent variables are obtained; from a set of algebraic equations, to the fourth order of accuracy, using an alternate-direction implicit (ADI) method as described in Ta Phouc Loc (1980) and in Bouhairie (2005). The temporal accuracy of the ADI scheme is second order. The calculations of the derivatives are implemented by a relaxation method in two sweeps. In the first sweep, the η-derivatives are determined by the Poisson equation

$$\lambda_{kh}\psi_{i,j}^{k+1/2} - \left(\frac{\partial^2\psi}{\partial\eta^2}\right)_{i,j}^{k+1/2} = -g_{i,j}\omega_{i,j}^{n} + \left(\frac{\partial^2\psi}{\partial\xi^2}\right)_{i,j}^{k} + \lambda_{kh}\psi_{i,j}^{k}, \tag{3.2}$$

and by a Hermitian relation in the η-direction,

$$\left(\frac{\partial^2\psi}{\partial\eta^2}\right)_{i,j-1}^{k+1/2} + 10\left(\frac{\partial^2\psi}{\partial\eta^2}\right)_{i,j}^{k+1/2} + \left(\frac{\partial^2\psi}{\partial\eta^2}\right)_{i,j+1}^{k+1/2} = \frac{12}{(\Delta\eta)^2}\left(\psi_{i,j-1}^{k+1/2} - 2\psi_{i,j}^{k+1/2} + \psi_{i,j+1}^{k+1/2}\right). \tag{3.3}$$

In the second sweep, the ξ-derivatives are determined again by the Poisson equation

$$\lambda_{kv}\psi_{i,j}^{k+1} - \left(\frac{\partial^2\psi}{\partial\xi^2}\right)_{i,j}^{k+1} = -g_{i,j}\omega_{i,j}^{n} + \left(\frac{\partial^2\psi}{\partial\eta^2}\right)_{i,j}^{k+1/2} + \lambda_{kv}\psi_{i,j}^{k+1/2} \tag{3.4}$$

and by the Hermitian relation in the ξ-direction,

$$\left(\frac{\partial^2\psi}{\partial\xi^2}\right)_{i-1,j}^{k+1} + 10\left(\frac{\partial^2\psi}{\partial\xi^2}\right)_{i,j}^{k+1} + \left(\frac{\partial^2\psi}{\partial\xi^2}\right)_{i+1,j}^{k+1} = \frac{12}{(\Delta\xi)^2}\left(\psi_{i-1,j}^{k+1} - 2\psi_{i,j}^{k+1} + \psi_{i+1,j}^{k+1}\right). \tag{3.5}$$

The first derivatives, for the velocity components U and V in (2.3), are also determined in two sweeps using the following Hermitian relations:

$$\left(\frac{\partial\psi}{\partial\xi}\right)_{i-1,j}^{k+1} + 4\left(\frac{\partial\psi}{\partial\xi}\right)_{i,j}^{k+1} + \left(\frac{\partial\psi}{\partial\xi}\right)_{i+1,j}^{k+1} = \frac{3}{(\Delta\xi)}\left(\psi_{i+1,j}^{k+1} - \psi_{i-1,j}^{k+1}\right), \tag{3.6}$$

$$\left(\frac{\partial\psi}{\partial\eta}\right)_{i,j-1}^{k+1} + 4\left(\frac{\partial\psi}{\partial\eta}\right)_{i,j}^{k+1} + \left(\frac{\partial\psi}{\partial\eta}\right)_{i,j+1}^{k+1} = \frac{3}{(\Delta\eta)}\left(\psi_{i,j+1}^{k+1} - \psi_{i,j-1}^{k+1}\right). \tag{3.7}$$

The relaxation coefficients λ_{kh} and λ_{kv} are introduced into the Poisson equations in the iteration for the derivatives.

The numerical solution starts with an irrotational flow. Initially, the vorticity is zero in the interior. However, the wall vorticity at the surface of the cylinder is not zero. As required by the no-slip boundary condition, this wall vorticity $\omega_{1,j}^{n+1}$ on the surface of the cylinder is determined by the following third-order condition (Ta Phouc Loc &

Bouard 1985):

$$\frac{12}{(\Delta\xi)^2}\psi_{2,j}^{n+1} - \frac{6}{(\Delta\xi)}\left(\frac{\partial\psi}{\partial\xi}\right)_{2,j}^{n+1} + \left(\frac{\partial^2\psi}{\partial\xi^2}\right)_{2,j}^{n+1} = g_{1,j}\omega_{1,j}^{n+1} + O(\Delta\xi^3). \tag{3.8}$$

Accurate evaluation of this wall vorticity ensures that the boundary-layer separations are correctly determined by the simulations. Once the wall vorticity $\omega_{1,j}^{n+1}$ has been determined by (3.8), the subsequent diffusion of this wall vorticity into the interior is determined by the advection–diffusion equation (2.4). A number of numerical schemes, based on the finite-volume formulation, have been employed to solve the advection–diffusion equation. Bouhairie (2005) gave details of the various numerical schemes and the numerical results obtained for each scheme in his PhD thesis. Only the reliable results obtained by the QUICK method (Leonard 1979; Hayase, Humphrey & Gerif 1992) are presented in this paper.

4. Computational grid and accuracy

The computation grid must have enough resolution within the viscous boundary layer that the heat-transfer rate can be computed accurately from the temperature gradient at the wall. The higher the Reynolds number, the thinner is the viscous layer and, subsequently, the finer is the requirement for the computation grid. The first cell of the computation grid next to the surface of the cylinder is rectangular in shape. The dimensions of this cell in the radial direction and in the tangential direction are selected to be equal to the front-stagnation-point (FSP) boundary-layer displacement thickness:

$$(\Delta r)_1 = a(\Delta\theta)_1 = \delta_1. \tag{4.1}$$

The FSP displacement thickness,

$$\delta_1 \simeq \frac{0.67}{\sqrt{Re}}a, \tag{4.2}$$

is a viscous length scale that is inversely proportional to the square root of the Reynolds number (Schlichting 1979). The linkage of the grid with the FSP displacement thickness ensures that the simulations correctly capture the flow characteristics on the surface of the cylinder. Many previous calculations of the flow used computational grids listed in columns 6–8 of table 3 which did not follow the rule given by (4.1). The result was a loss of resolution when a grid coarser than δ_1 was used at higher Reynolds numbers.

Figure 1 shows the computation grid used in a flow simulation at Reynolds number $Re = 1000$. In the transformed domain, defined by $0 < \xi < \xi_\infty$ and $0 < \eta < 2$, the computation was conducted using a uniform grid of mesh size

$$\Delta\xi = \frac{\xi_\infty}{I_m}, \qquad \Delta\eta = \frac{2}{J_m}. \tag{4.3}$$

Since the mesh size in the polar coordinates and the mesh size in the transformed coordinates are related by

$$(\Delta r)_1 \simeq a\pi\Delta\xi \simeq \delta_1, \qquad \Delta\theta = \pi\Delta\eta, \tag{4.4}$$

the number of computational grid points is

$$I_m = \frac{\xi_\infty}{\Delta\xi} = \pi\frac{a}{\delta_1}\xi_\infty = 4.7\sqrt{Re}\,\xi_\infty, \qquad J_m = 2I_m. \tag{4.5}$$

Authors	Dimension	Re	θ_s (deg.)	St	Grid	$(\Delta r)_1$	$a(\Delta\theta)_1$
Present simulation results	2D	200	111 ± 2	0.190	70×140	δ_1	δ_1
		300	110.5 ± 4.5	0.200	82×164	δ_1	δ_1
		1000	102 ± 9	0.232	75×150	$2\delta_1$	$2\delta_1$
			102 ± 8	0.224	150×300	δ_1	δ_1
			103 ± 8	0.222	300×600	$\frac{1}{2}\delta_1$	$\frac{1}{2}\delta_1$
		5000	90 ± 6	0.228	340×680	δ_1	δ_1
		8290	92.5 ± 9.5	0.224	430×860	δ_1	δ_1
		15 550	86.5 ± 6.5	0.210	600×1200	δ_1	δ_1
Chou & Huang (1996)	2D	1000	99.6 ± 6	0.220	129×121	$1.2\delta_1$	$2.5\delta_1$
		40 000	83.1 ± 8	0.220	193×241	$7.8\delta_1$	$4.9\delta_1$
Thoman & Szewczyk (1969)	2D	200	116	0.150	$\simeq 24 \times 36$	$0.25\delta_1$	$3.7\delta_1$
		600	113	—	$\simeq 24 \times 36$	$0.25\delta_1$	$6.4\delta_1$
		40 000	83	0.170	$\simeq 24 \times 36$	$0.25\delta_1$	$52.\delta_1$
Persillon & Braza (1998)	2D	100	113.5	0.165	213×102	$1.4\delta_1$	$1.4\delta_1$
		200	109.5	0.198	213×102	$2.0\delta_1$	$2.0\delta_1$
		300	109.4	0.209	213×102	$2.5\delta_1$	$2.5\delta_1$
Persillon & Braza (1998)	3D	100	113.3	0.164	$213 \times 102 \times 32$	$1.4\delta_1$	$1.4\delta_1$
		200	107.9	0.181	$213 \times 102 \times 32$	$2.0\delta_1$	$2.0\delta_1$
		300	106.5	0.206	$213 \times 102 \times 32$	$2.5\delta_1$	$2.5\delta_1$

TABLE 3. Global parameters and computational grids of the present and previous simulations. 2D, two-dimensional grid; 3D, three-dimensional grid.

The calculations presented in this paper use $\xi_\infty = 1$, which sets the outflow boundary at approximately 23 radii from the cylinder. Extending the boundary further from 23 radii to 180 radii produces no significant difference in the flow characteristics near the surface of the cylinder (Bouhairie 2005). To assure stability of the numerical calculation, the dimensionless time step in the calculations, $\Delta t = U\Delta\tilde{t}/a$, is selected so that the Courant number $U\Delta\tilde{t}/(\Delta r)_1 \simeq 0.5$.

Calculations were also carried out using a coarser grid and a finer grid at Reynolds number $Re = 1000$. The results of this grid-refinement study are given in table 3 and in table 5 in a later section. With two-fold and four-fold grid refinement, the changes in the values of the parameters such as the Strouhal number, the angle of separation, the Nusselt number, the front-to-back heat-transfer ratio etc. vary by only a few percent. These results have given confidence to our criteria for grid selection.

5. Vorticity and temperature distributions

The sequence of the vorticity and temperature maps obtained from the numerical computation at $Re = 15\,550$ is shown in figure 2 for dimensionless times $t = 99.0$, 99.5, 100.0. These maps illustrate the development of the unsteady viscous boundary layers and the separation of the viscous layers from the surface of the cylinder. There are many points of flow separation, and they are marked on the vorticity maps by the arrows pointing to the vorticity zeros on the surface of the cylinder. The number of zeros changes with time from 13 zeros at time $t = 99$ to 15 zeros at time $t = 99.5$ and then back to 13 zeros at time $t = 100$. The number of zeros increases by 2 whenever an eddy is generated. The number decreases by 2 when an eddy is detached from the surface. The eddies are defined by pairs of vorticity zeros on the surface of the cylinder. The locations of these zeros change with time as the wake moves laterally

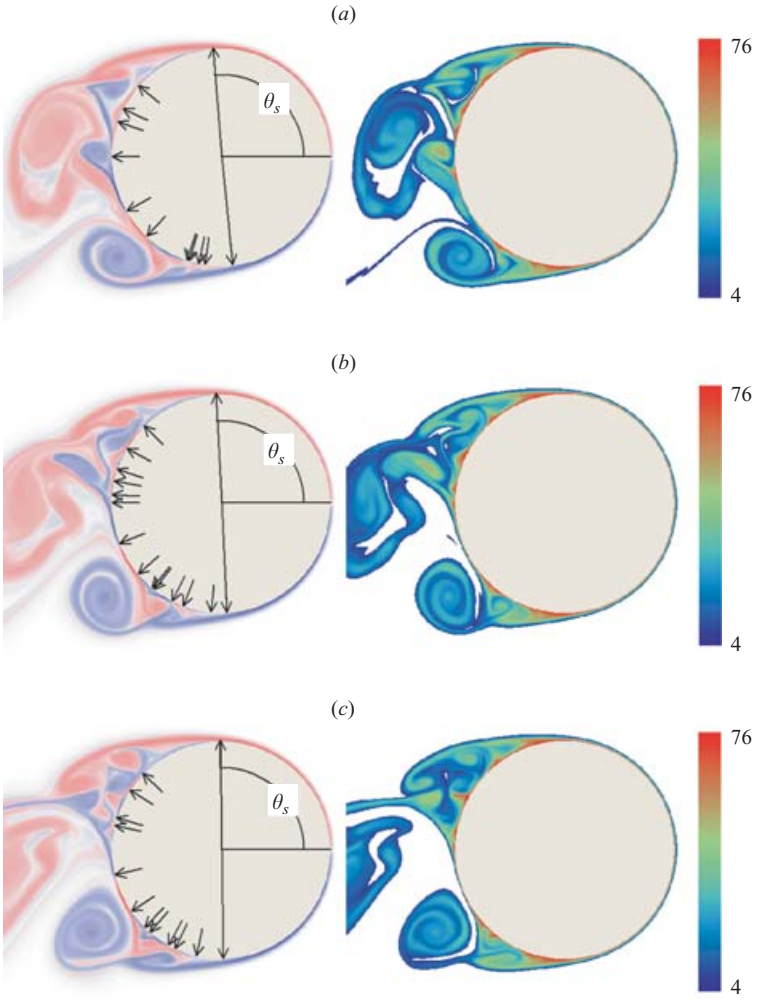

FIGURE 2. Vorticity maps (left) and temperature maps (right) at (*a*) $t = 99.0$, (*b*) 99.5, (*c*) 100.0 for $Re = 15\,550$. Positive vorticity is shown in red and negative in blue. The arrows mark the points of zero vorticity on the surface of the cylinder. The color bars define the temperature from $T = 76\,^{\circ}\mathrm{C}$ to $T = 4\,^{\circ}\mathrm{C}$. The area where $T < 4\,^{\circ}\mathrm{C}$ is shown as white.

from side to side. The eddies are continuously generated and then detached from the back surface of the cylinder. The release of vorticity into the wake is by detachment of the eddies.

The thermal energy is released along thread-like pathways, which hereafter are referred to as 'flares', at locations close to but not exactly at the points of zero vorticity. The temperature maps in figure 3 show close-up views of the flares on the back surface of the cylinder for four flows with Reynolds numbers $Re = 1000$, 5000, 8290 and 15 550. The width of the flares is defined between isotherms where the temperature is equal to one-half the wall value. As marked by the two-way arrows in these close-ups, the width of the flares is

$$w \simeq 7\delta_1. \tag{5.1}$$

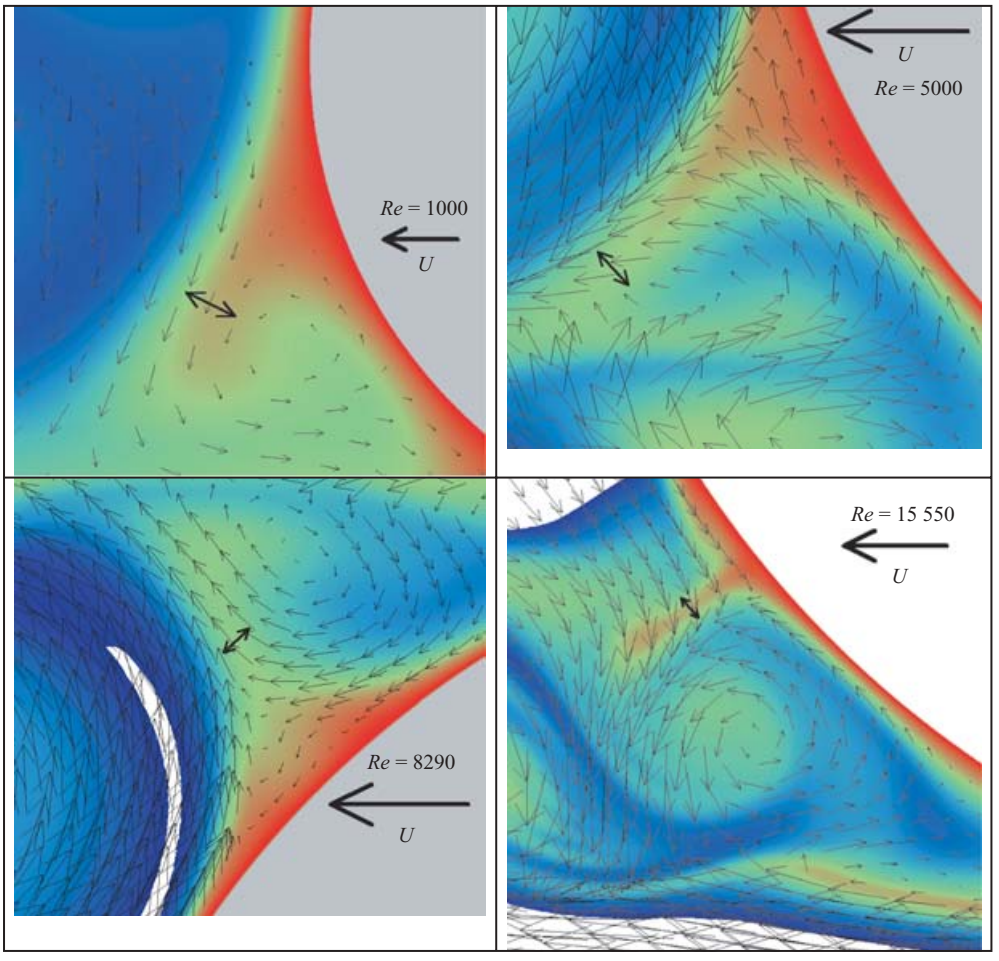

FIGURE 3. Flare-up of thermal energy (red) on the back surface of the circular cylinder for $Re = 1000$, 5000, 8290 and 15 550. The thick arrow to the right indicates the magnitude of the crossflow velocity. The width of the flare is indicated by the double-ended arrow, the length of which is equal to seven times the FSP thickness.

The tangential velocity near the surface of the cylinder changes direction at the points of flow separation, where the surface vorticity is zero, $\partial v_\theta/\partial r \simeq 0$. However, the flare-up of thermal energy is associated with the tangential gradient of the tangential velocity, $\partial v_\theta/\partial\theta$, which changes sign at locations that do not coincide with the points of flow separation, where the vorticity is zero. On average, the number of flow-separation points is approximately equal to the number of flares.

The circumferential distribution of the wall vorticity on the surface of the cylinder obtained from the simulations is shown in figures 4(a–c) for Reynolds number $Re = 200$, 5000 and 15 550. The eddies attached to the surface of the cylinder are defined by the magnitude of the vorticity maxima and the location of the vorticity zeros in these profiles. The magnitude of the vorticity maxima increases with the Reynolds number. The number of zeros also increases with the Reynolds number. For $Re = 200$ (see figure 4a), the maxima occur in the viscous boundary layer, where $\theta \simeq 50^\circ$ and 310°. At this instant, $t = 100$, there are three locations where the vorticity

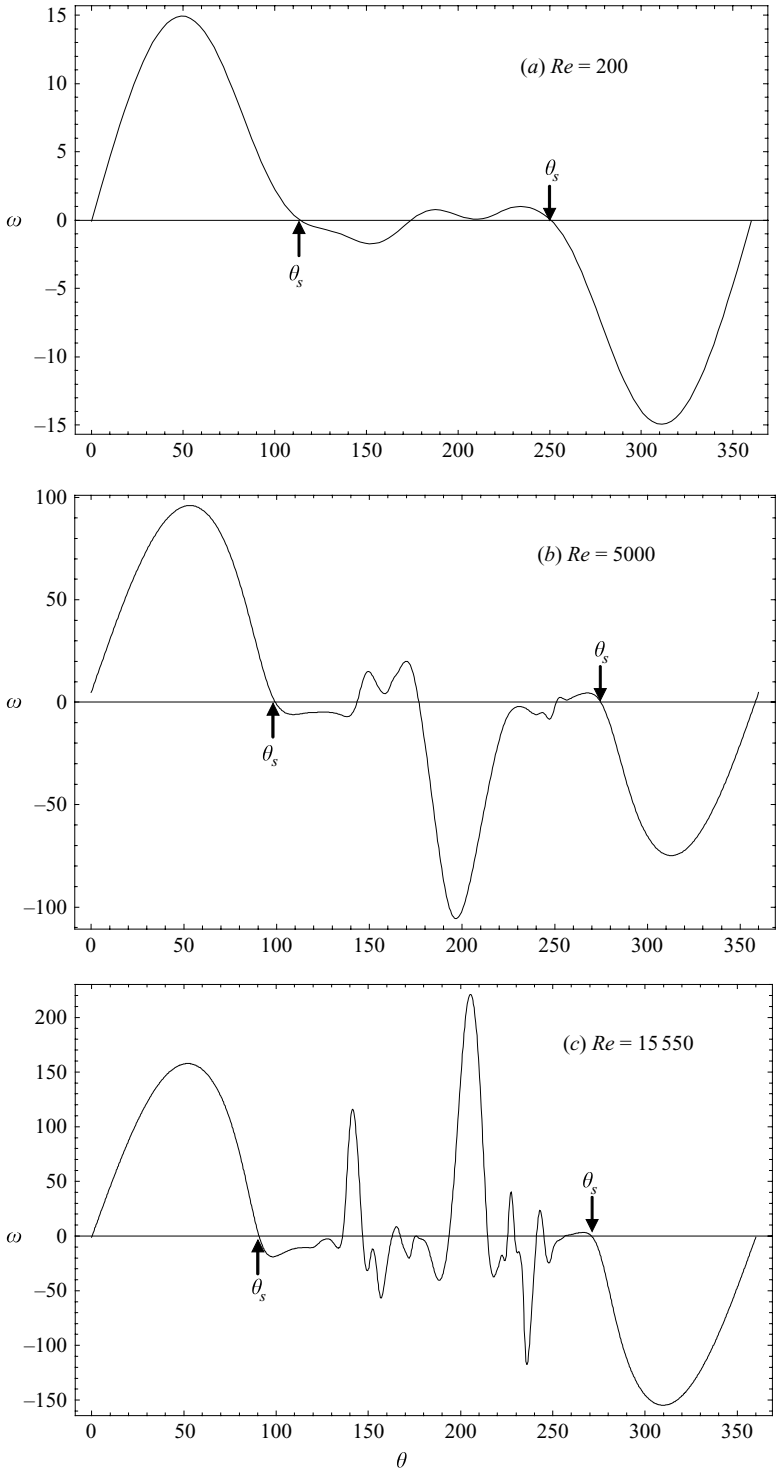

FIGURE 4. Wall-vorticity profiles at time $t = 100$ for Re (*a*) 200, (*b*) 5000, and (*c*) 15 550. The initial boundary-layer separation is indicated by arrows pointing to the first pair of vorticity zeros. The front stagnation point is located at $\theta = 0^\circ = 360^\circ$.

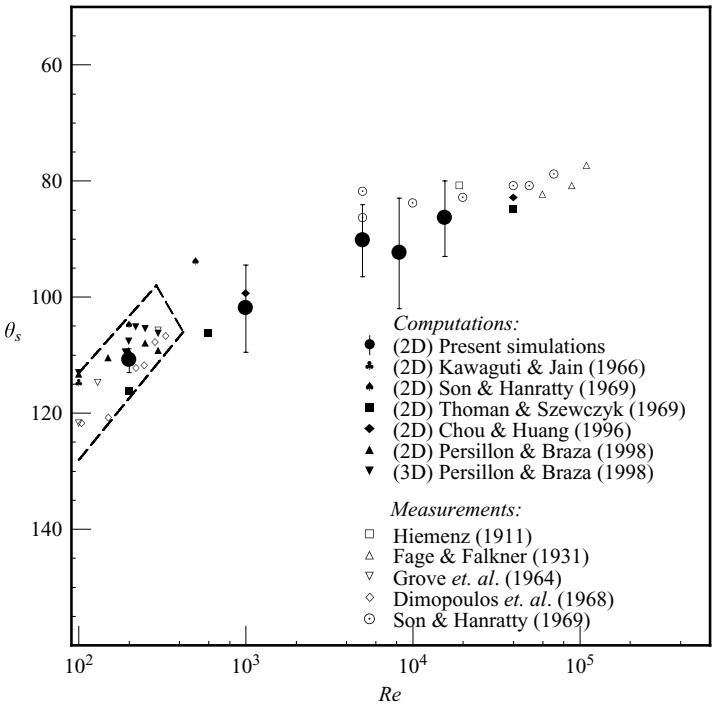

FIGURE 5. Angles of the initial boundary-layer separation. The solid symbols denote the results of the numerical simulation while the open symbols denote laboratory measurements.

is zero. Two of the vorticity zeros occur at the extreme angles $\theta_s = 110°$ and 250°. These are the locations associated with the initial separation of the viscous layer. Only one vorticity zero occurs on the back surface, at $\theta \simeq 175°$, at this time and for this Reynolds number. At the higher Reynolds numbers of $Re = 5000$ and 15 550 (see figures 4*b* and 4*c*), the wall vorticity at locations on the back surface can become higher than the value along the side. The high vorticity intensity is due to a steep tangential-velocity gradient, $\partial v_\theta / \partial r$, within an unsteady viscous layer of small thickness on the back surface. The viscous layers on the back are highly unsteady and, unlike the boundary layer, they develop from the front but play the same role in keeping the vorticity and thermal energy close to the wall. Separation of the viscous layers occurs at the locations where the vorticity is zero. From now on in this paper, 'viscous layers' are taken to be boundary layers on the back surface of the cylinder. The term is generalized to describe the regions of thermal energy and vorticity entrapment close to the surface of the cylinder, while 'separations' refers to the disruption of these viscous layers from positions close to the surface.

6. Initial boundary-layer separation

The initial separation of the boundary layer is defined by the first pair of vorticity zeros on the surface of the cylinder. The angle of this initial separation is θ_s, as indicated in figure 4. The same angle is defined also by the arrows in figure 2. Since the process of separation is asymmetric and unsteady, the point of this first vorticity zero moves back and forth along the back surface. The angle θ_s on one side of the cylinder is different from that on the other side. The angle also oscillates with time. The range of this oscillation and the average value of the angle for Reynolds numbers $Re = 200$, 1000, 5000, 8290 and 15 550 are shown in figure 5 and table 3. In the figure,

the vertical lines define the range and the large solid symbols denote the averaged value.

There are many previous experimental data available for comparison with the present simulation results. In the laboratory experiments, the angle θ_s was the location where the vorticity is on the average close to zero. It was difficult physically to measure the vorticity at the wall with acceptable accuracy. Using a Stanton tube, Fage & Falkner (1931) measured the near-surface velocities to find the intensity of the wall friction. The point where the frictional intensity falls to zero defined the separation of the boundary layer. They admitted that reliable measurements of the friction with the Stanton tube could be obtained only when the boundary layer was not too thin compared with the diameter of the Stanton tube. This condition was not satisfied for flow with large Reynolds numbers. Grove *et al.* (1964) measured the pressure profile on the cylinder surface using a manometer and located the point of separation by the pressure gradient. They noted that the measurements were not entirely reliable since the flows were unsteady at their range of Reynolds numbers, varying from $Re = 30$ to 300. The measurements using the Stanton tube and a pressure tap connected to the manometer gave only an average value.

Although flow separation may be defined at points where the wall friction is zero, the location of this zero friction is not possible because the wall friction at a location is zero only at one instant of time. The average of the wall friction over time is not in fact zero anywhere on the surface of the cylinder. Son & Hanratty (1969) obtained the wall friction by electrochemical measurements, which were more accurate than calculations based on measured pressure profiles. However, since the average of the wall friction was non-zero, they had to locate the separation angle at the point where the average friction is a minimum. Despite the improved accuracy in their friction measurements, the angle at minimum friction was not determined with certainty, since this minimum is not sharply defined but occurs over a range of angles.

In numerical simulations, the first point of zero vorticity accurately defines the boundary-layer separation. However, the location of this first vorticity zero depends on the numerical method and the resolution of the numerical grid. The earlier simulation of the flow at $Re = 200$ to 40 000 by Thoman & Szewczyk (1969) was based on first-order upwinding and a relatively coarse grid (see table 3). The mesh size of the cell next to the wall used by Thoman & Szewczyk (1969) was $(\Delta r)_1 \simeq \frac{1}{4}\delta_1$ and $\Delta\theta = 10°$. The thickness of their highly elongated cell is sufficiently small. However, the lateral dimension of this cell in the θ-direction was fixed at 10°, which is exceedingly large compared with the desired $a(\Delta\theta)_1$; this would be a much smaller value, $360°/1880 \simeq 0.2°$, if the calculation were carried out using the present method at $Re = 40\,000$.

The results of the present simulation are in agreement with the recent results of Chou & Huang (1996). This two-dimensional simulation by Chou and Huang was conducted using a curvilinear grid of comparable resolution. At Reynolds number $Re = 40\,000$, the number of cells in our refined grid would be 940×1880. This may be compared with the grid of 193×241 used by Chou & Huang (1996) and the grid of 24×36 used by Thoman & Szewczyk (1969). Three-dimensional direct numerical simulation of the flow was carried out by Persillon & Braza (1998) up to $Re = 300$. They also conducted two-dimensional simulations using a grid of similar resolution to ours. Their two-dimensional, as well as their three-dimensional, results can be seen from figure 5 to agree with the present numerical results. In their Reynolds number range, varying from $Re = 100$ to 300, there was a three-dimensional effect on the drag coefficient and the Strouhal number. However, the three-dimensional effect on the initial angle of the boundary-layer separation is apparently not as significant.

The difference between the two-dimensional and three-dimensional simulations is $\Delta\theta_s = 0.2^\circ$ for $Re = 100$, $\Delta\theta_s = 1.6^\circ$ for $Re = 200$ and $\Delta\theta_s = 2.9^\circ$ for $Re = 300$. The two-dimensional simulations give slightly higher values in this range of Reynolds numbers (see table 3).

7. Eddies on the surface of the cylinder

The number of vorticity zeros defines the points of separation and the number of eddies on the surface of the cylinder. This information is given in panel (*a*) of figures 6–9 for $Re = 1000$, 5000 and 15 550. The loci of the vorticity zeros trace lines over space and time in these figures. The outer envelope of the loci defines the initial angle of the boundary-layer separation, $\theta_s(t)$, which is a function of time. The frequency associated with this initial separation, f, is determined by counting the number of oscillations of this outer envelope over the period of time from $t = 30$ to 100. The dimensionless number of this primary frequency is the Strouhal number $St = fD/U_\infty$, which as shown in figure 10 is a function of the Reynolds number. In the Reynolds-number range from $Re = 200$ to 300, the present simulation results are in agreement with the experimental data and are in between the two-dimensional and three-dimensional simulation results of Persillon & Braza (1998). The frequency obtained from the two-dimensional simulation by them is higher than the average of the experimental data. The frequency obtained from the three-dimensional simulation by Persillon & Braza (1998), however, was slightly lower than the average of the experimental data in this range of the Reynolds number. Persillon and Braza attributed the drop in frequency around $Re = 200$ to a three-dimensional effect. At higher Reynolds numbers, in the range between $Re = 1000$ to 40 000, both the present numerical simulation and the two-dimensional simulation of Chou & Huang (1996) give slightly higher values than the average of the experimental data. However, the Strouhal number obtained from the present simulation for Reynolds number $Re = 15\,550$ is equal to the average of the experimental data.

Due to phase jitter, the frequency of oscillation is not exactly constant. The present calculations of the Strouhal number were based on averages over a period of time ($t \simeq 30 \sim 100$) corresponding to approximately nine cycles of oscillations. This small number of cycles causes errors that can be comparable with the scatter of the experimental data. Nevertheless, the trend of the present simulation results is consistent with experiment and with other numerical results as shown in figure 10.

At high Reynolds numbers, there are many vorticity zeros between the initial angles of separation. The population number of these vorticity zeros on the surface of the cylinder at each instant of time is counted from the loci shown in panel (*a*) of figures 6–9. This number, n_ω, changes with time as shown in figure 11. The change in this number n_ω with time is typically 2 units. An increase in the number by 2 signals the creation of an eddy, while a decrease by 2 signals the detachment of an eddy from the wall. The total number of eddies attached to the wall is $\overline{n}_E = \overline{n}_\omega - 1$. Over the period from times $t = 30$ to 100, the averaged numbers of the vorticity zeros are $\overline{n}_E = 6.5 - 1$, as shown in figure 11(*a*), for $Re = 1000$ and $\overline{n}_E = 14.1 - 1$, as shown in figure 11(*b*), for $Re = 15\,550$. This eddy population number $\overline{n}_E$ increases with the Reynolds number, as shown in figure 12(*a*). The data in the figure approximately fit the relation

$$\overline{n}_E \simeq 0.107 Re^{1/2}. \tag{7.1}$$

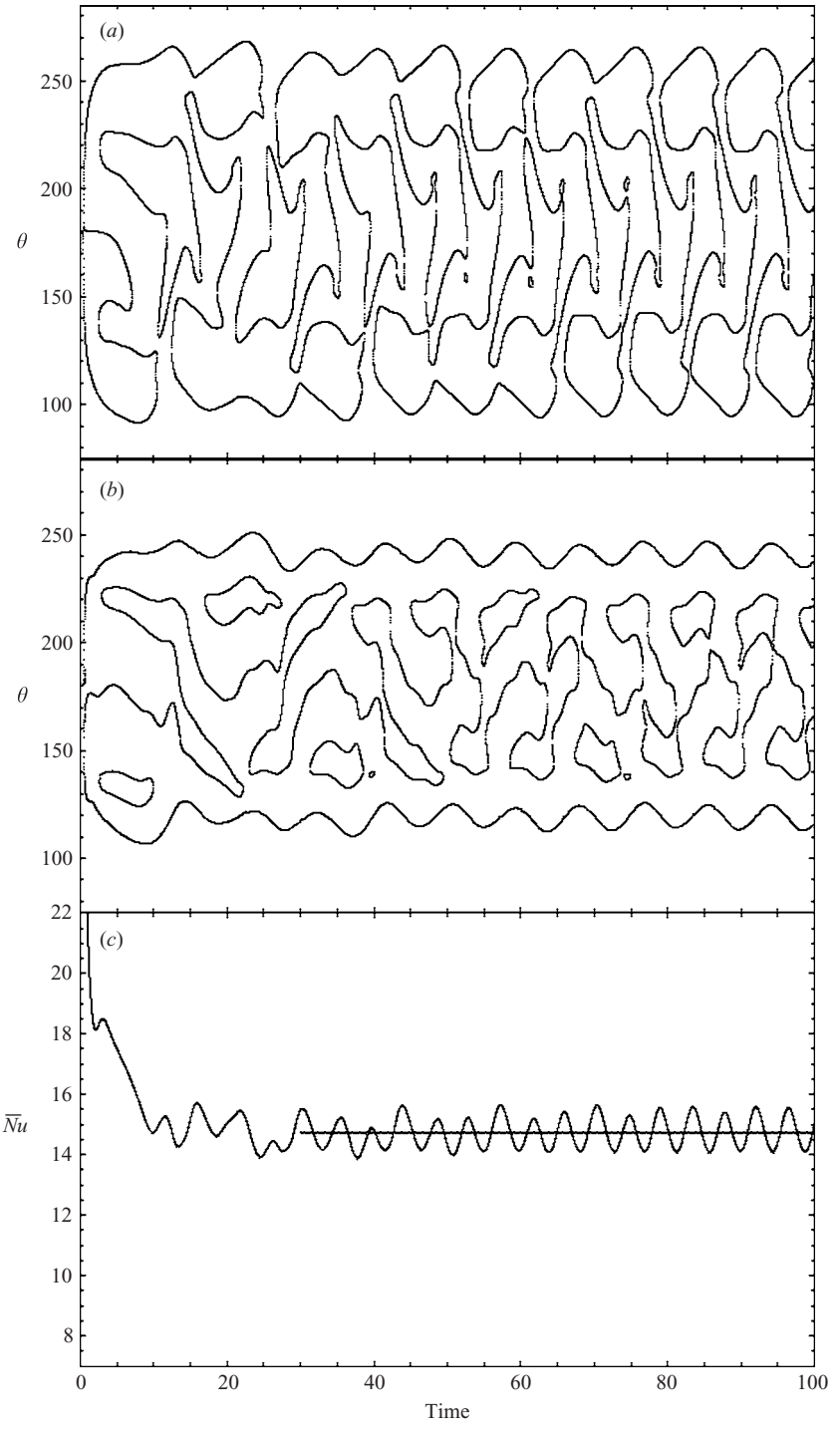

FIGURE 6. (*a*) Loci of the vorticity zeros, (*b*) loci of the *Nu* minima and maxima and (*c*) the circumferential average Nusselt number $\tilde{N}u$ vs. time at $Re = 1000$.

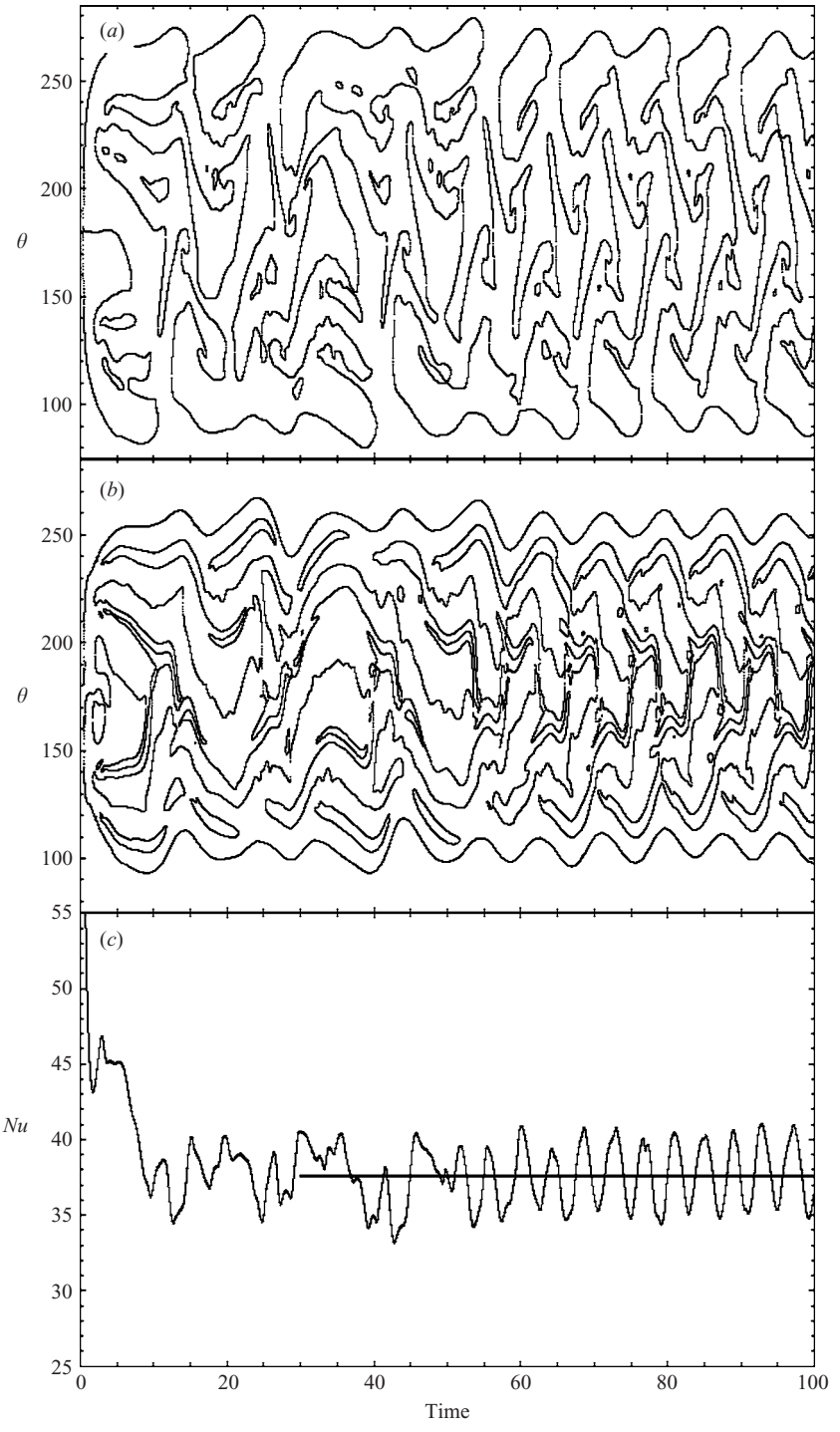

FIGURE 7. (*a*) Loci of the vorticity zeros, (*b*) loci of the *Nu* minima and maxima and (*c*) the circumferential average Nusselt number $\tilde{N}u$ vs. time at $Re = 5000$.

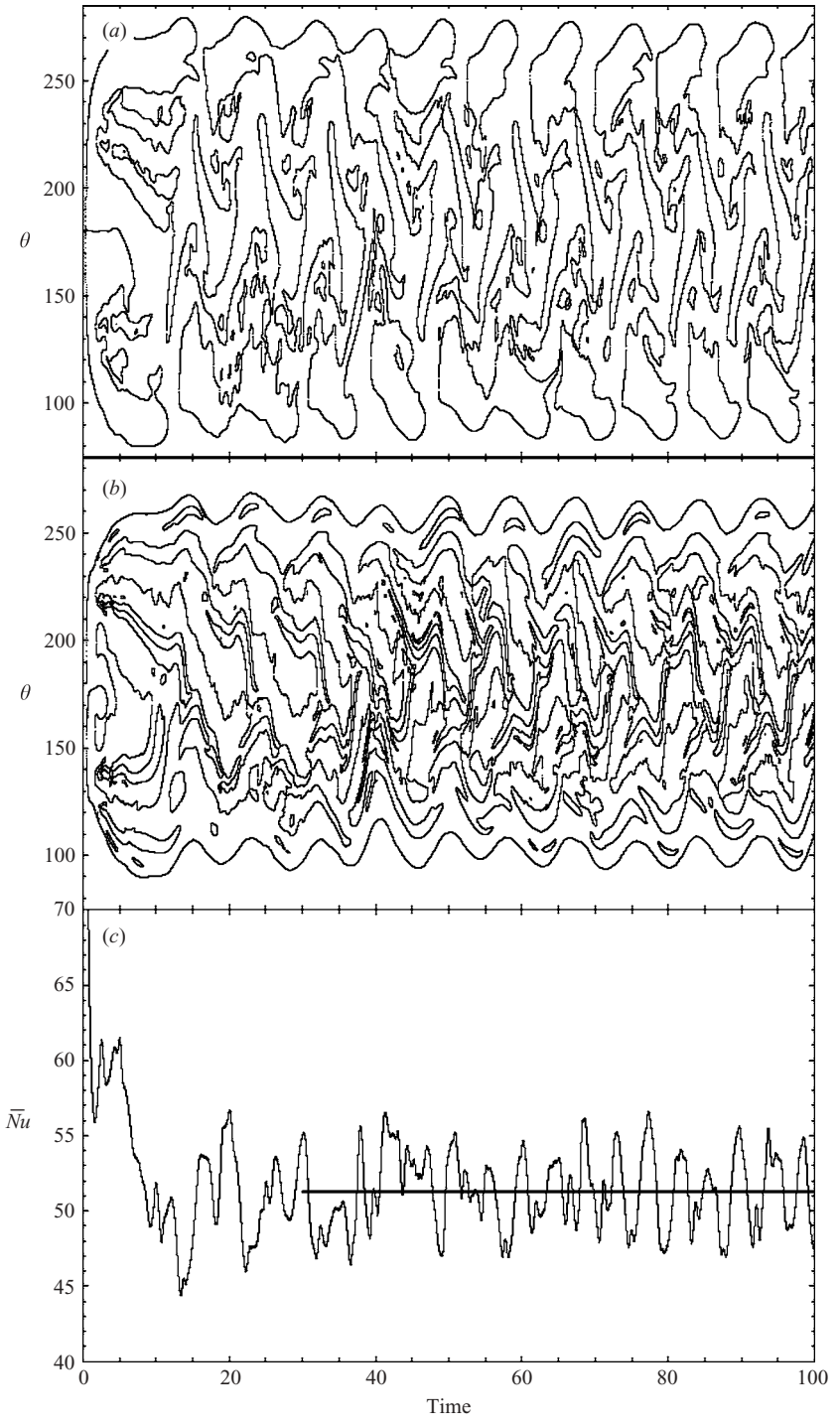

FIGURE 8. (*a*) Loci of the vorticity zeros, (*b*) loci of the *Nu* minima and maxima and (*c*) the circumferential average Nusselt number $\tilde{Nu}$ vs. time at $Re = 8290$.

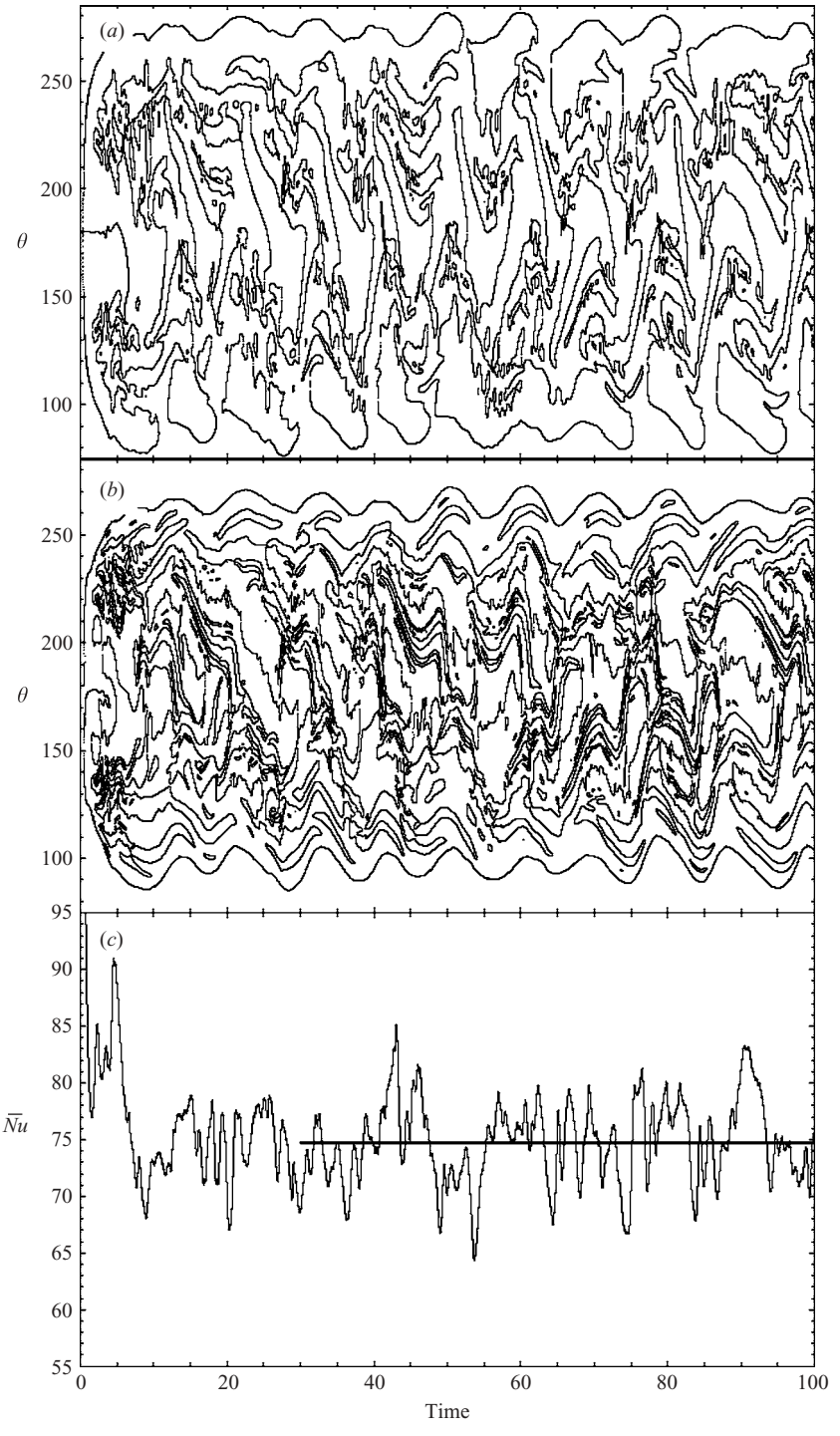

FIGURE 9. (*a*) Loci of the vorticity zeros, (*b*) loci of the *Nu* minima and maxima and (*c*) the circumferential average Nusselt number $\tilde{N}u$ vs. time at $Re = 15\,550$.

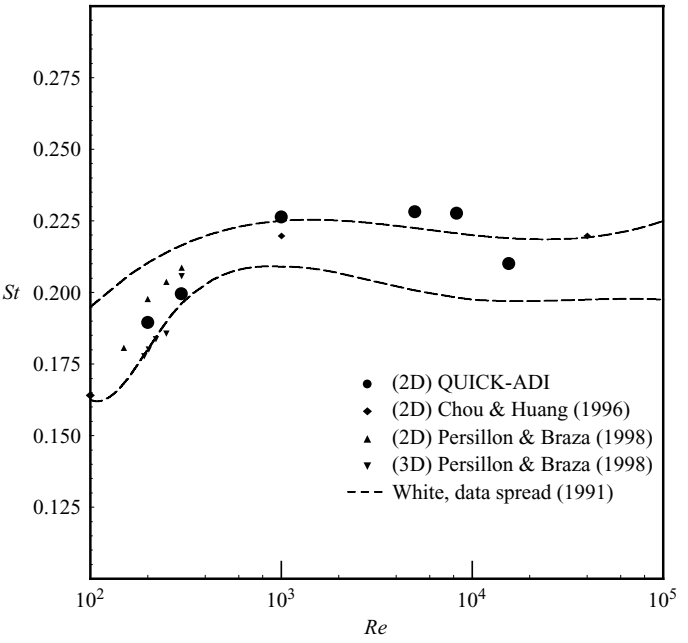

FIGURE 10. The Strouhal number St associated with vortex shedding of the primary eddy. The dashed lines defines the range of the experimental data.

The average spacing between eddies is the arclength πa divided by the population number $\overline{n}_E$. Since $\delta_1 = 0.67aRe^{-1/2}$,

$$\lambda_E = \frac{\pi a}{\overline{n}_E} \simeq 44\delta_1. \tag{7.2}$$

According to this equation the space between eddies, λ_E, is approximately equal to $44\delta_1$.

The eddy-detachment frequency f_E also increases as the population number $\overline{n}_E$; both increase with the Reynolds number. The dimensionless number corresponding to this eddy-detachment frequency is the eddy Strouhal number, $St_E = f_E D/U_\infty$, which increases with the Reynolds number, following approximately the linear relation

$$St_E \simeq 0.000\,735\,Re, \tag{7.3}$$

as shown in figure 12(b). This eddy Strouhal number St_E is the result of all eddies large and small, detached from the surface. At high Reynolds numbers, the Strouhal number of the main eddy approaches the asymptotic value $St \simeq 0.2$, as shown in figure 10. However, the eddy Strouhal number of all detached eddies, St_E, increases with Reynolds number without bound. Equation (7.3) may be rewritten in the form

$$\frac{f_E \nu}{U_\infty^2} \simeq 0.000\,735, \tag{7.4}$$

which suggests that the detachment frequency of the eddies depends on the viscous time scale ν/U_∞^2 and not on the size of the cylinder. At high Reynolds numbers, the vorticity is trapped in the viscous layers close to the wall. The release of the vorticity through the detachment of eddies from the wall is a localized process that may not depend on the size of the cylinder.

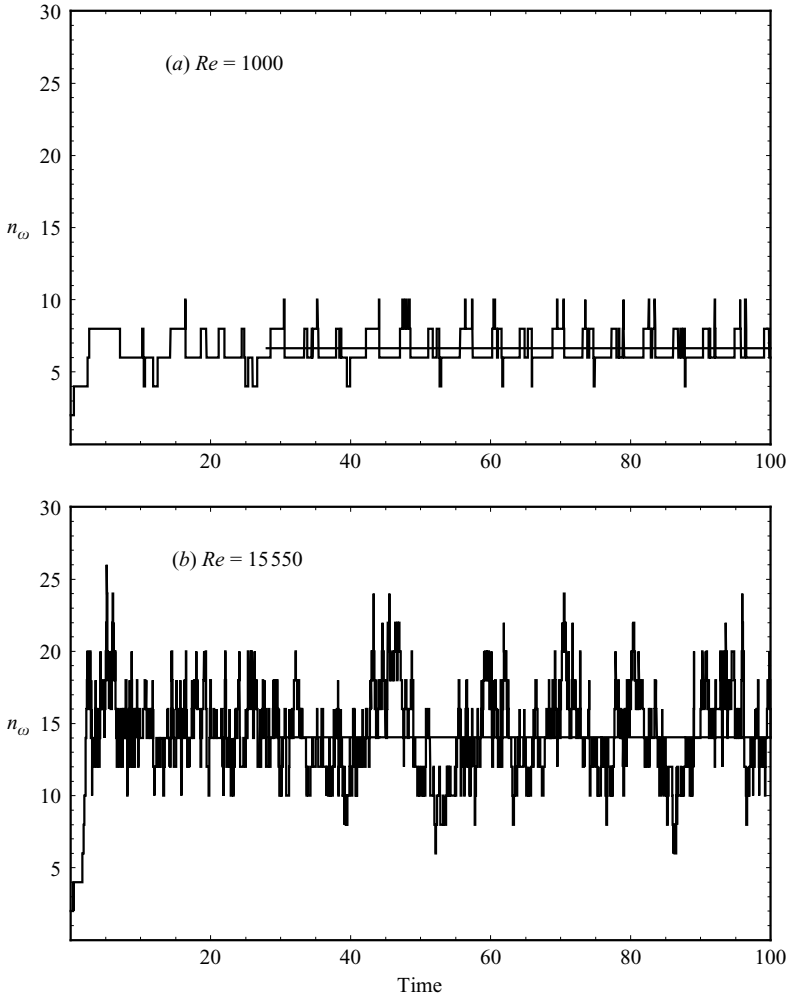

FIGURE 11. Variation in the number of vorticity zeros with time for two flows, with Reynolds number (*a*) $Re = 1000$ and (*b*) $Re = 15\,550$. The averages over the period from $t = 30$ to 100 are $\overline{n}_\omega = 6.7$ for $Re = 1000$ and $\overline{n}_\omega = 14.1$ for $Re = 15\,550$.

8. Nusselt number and thermal-boundary-layer thickness

The release of thermal energy follows a similar process to the vorticity. The thermal energy is trapped in the viscous layers close to the wall and subsequently released by the detachment of eddies from the wall. The heat flux from the wall of the cylinder is

$$q = -k\left(\frac{\partial T}{\partial r}\right)_{r=a} = -k\frac{T_\infty - T_w}{\delta_T}, \tag{8.1}$$

which is the product of the heat-conduction coefficient k- and the temperature gradient at the wall, $(\partial T/\partial r)_{r=a}$. The length scale of this heat flux is the thermal-boundary-layer thickness

$$\delta_T = \frac{T_\infty - T_w}{(\partial T/\partial r)_{r=a}}, \tag{8.2}$$

which is defined by the temperature difference across the layer, $T_w - T_\infty$, and the temperature gradient at the wall. The dimensionless parameter of the heat flux q is

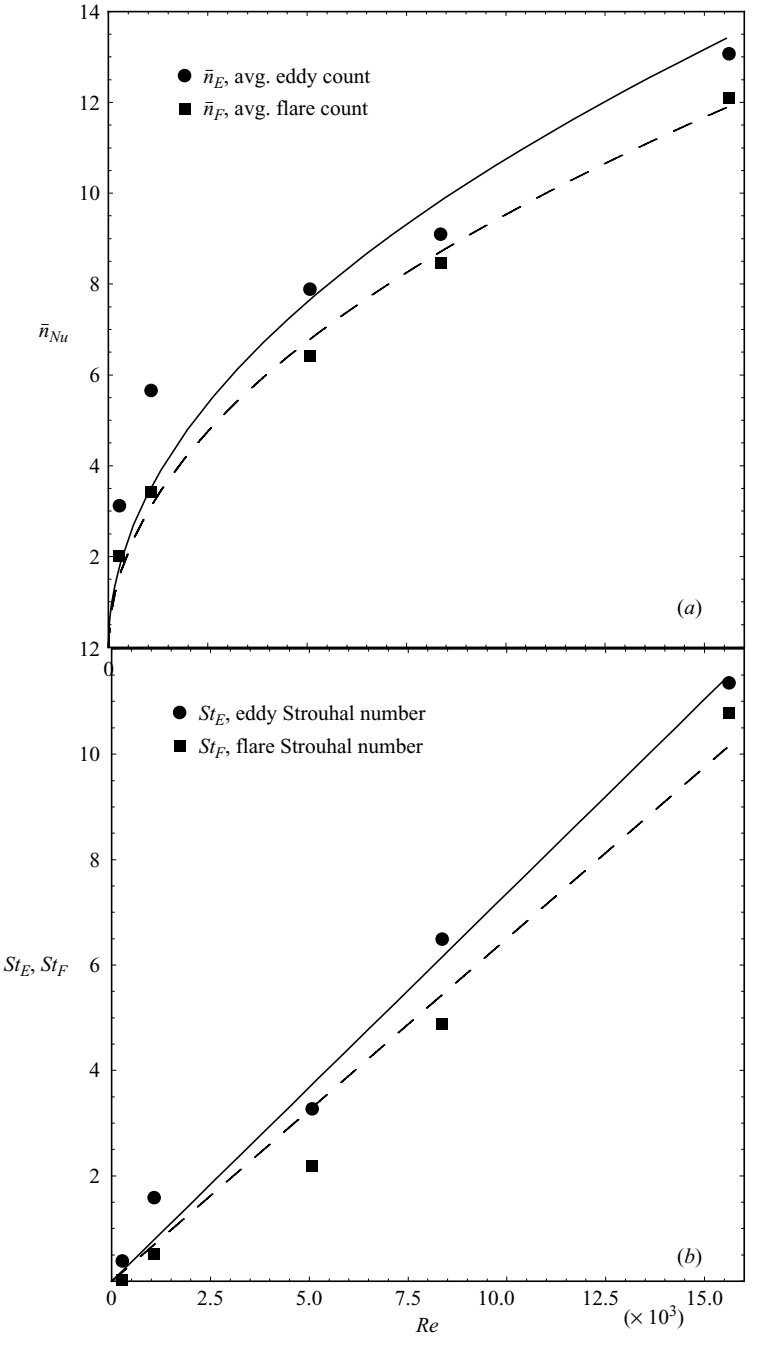

FIGURE 12. (*a*) Population numbers of eddies and flares on the back surface, $\overline{n}_E$ and $\overline{n}_F$. (*b*) Strouhal numbers of eddies and flares, St_E and St_F.

the Nusselt number,

$$Nu = \frac{qD}{k(T_w - T_\infty)} = \frac{D}{\delta_T}, \tag{8.3}$$

which may be interpreted as a length-scale ratio of D and δ_T. Figures 13(*a*), (*b*) and (*c*) show the circumferential profiles $Nu(\theta)$ of this Nusselt number obtained from the

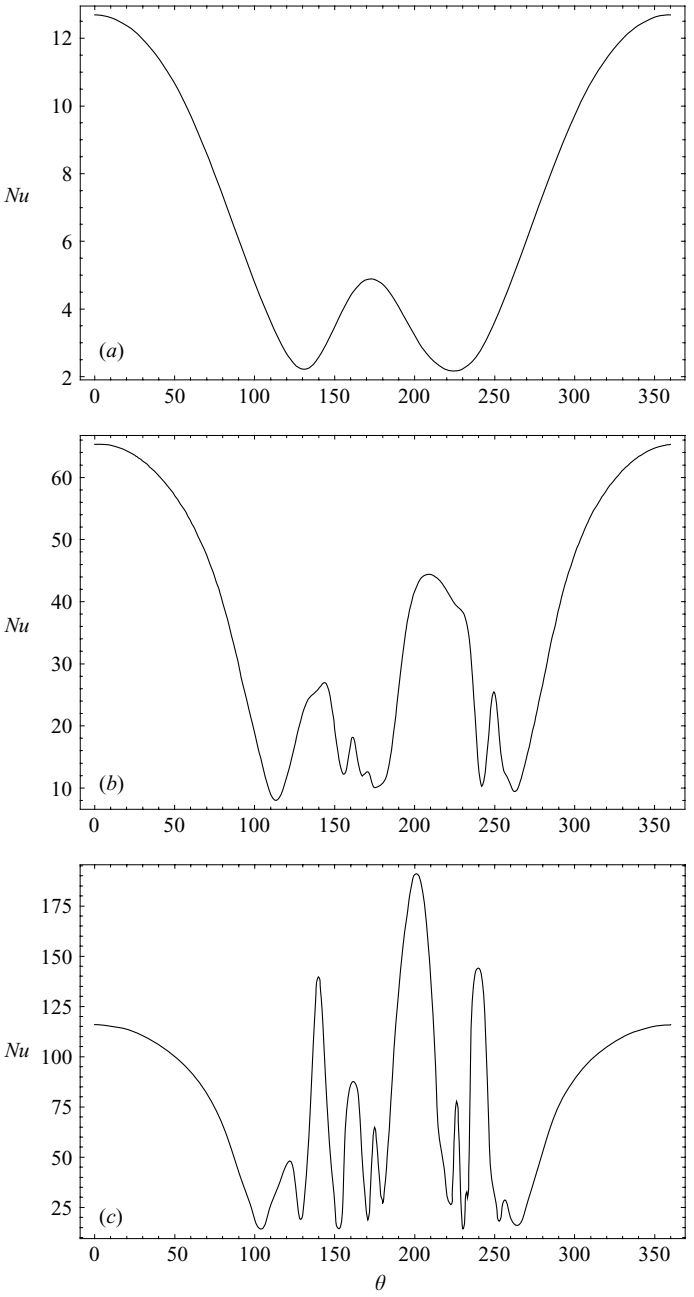

FIGURE 13. Circumferential profile of the Nusselt number at the instant of time $t = 100$ for Reynolds numbers (*a*) $Re = 200$, (*b*) 5000, (*c*) 15 550.

simulations at one instant of time, $t = 100$, for Reynolds numbers $Re = 200$, 5000 and 15 550. The maxima and the minima of these profiles define the thermal structure on the surface of the cylinder. The maxima are associated with the steep temperature gradient in the viscous layer. The minima are due to the flares of thermal energy, which are narrow pathways directed away from the wall, as shown in figure 3. The

		Overall $\overline{Nu}$				Stagnation Nu_s				
Re	$\theta_{Nu_{min}}$		3D X&K	2D K	Exp E&D		Exp S&W	BL F	Exp S	*R* (%)
200	$132° \pm 4°$	**6.55**		8.3	6.58	**12.7**	—	13.4	14.0	**13.2**
500	—		12.5		11.6	—	—		22.1	
1000	$118.5° \pm 6.5°$	**14.7**			14.3	**26.5**	—	30.0	31.3	**21.0**
3900	—		50.0		35.7				61.8	
5000	$103.5° \pm 5.5°$	**37.7**			36.4	**65.0**	—	67.2	70.0	**31.1**
8290	$101.5° \pm 7.5°$	**51.4**			49.3	**84.2**	91.3	89.5	90.1	**34.8**
15 550	$95.5° \pm 6.5°$	**74.8**			71.9	**115**	119	118	123	**40.5**

TABLE 4. Heat-transfer parameters obtained from the simulations and the experimental observations for comparison. The bold-face values are the results of the present calculations. Exp, experiment; 2D, two-dimensional; 3D, three-dimensional; BL, boundary-layer; X&K, Xia & Karniadakis (1997); K, Karniadakis (1988); E&D, Eckert & Drake (1972); S&W, Schmidt & Wenner (1943); F, Frossling (1958); S, Squire (1938).

population number of the flares on the back surface, n_F, is determined by counting the number of minima in these profiles (see figure 12).

9. Front-stagnation heat transfer

One location of the Nusselt-number maxima occurs at the cylinder's front stagnation point (FSP). As shown in figures 13(*a*)–(*c*), the values of the Nusselt number at the FSP are $Nu_s = 12.7$, 65.0 and 115, for Reynolds numbers $Re = 200$, 5000 and 15 550, respectively. Table 4 and figure 14 summarize the data obtained for Nu_s from the present simulations and the previous simulations and experiments. The boundary-layer calculations by Frossling (1958) give values 3 %–6 % higher than those of the present results. The laboratory measurements by Schmidt and Wenner (1943) of Nu_s at $Re = 8390$ and 15 550 also give values that are slightly higher, about 6 %. On the whole, the simulation results and the experimental data fit the formula

$$Nu_s = 0.92 Re^{1/2} \tag{9.1}$$

for the present range of Reynolds numbers. Such a relation with the Reynolds number suggests that the heat-transfer rate is proportional to the FSP thickness δ_1. Since $\delta_1 = 0.67 a Re^{-0.5}$,

$$Nu_s = \frac{D}{(\delta_T)_s} = 0.616 \frac{a}{\delta_1}. \tag{9.2}$$

According to this formula, the thermal boundary-layer thickness at the FSP is

$$(\delta_T)_s = 3.25 \delta_1. \tag{9.3}$$

Since the wall-mesh sizes are $(\Delta r)_1 = a(\Delta\theta)_1 = \delta_1$, the thermal structures are resolved in the present simulations by approximately three nodes within the boundary layer. Most previous computations used coarser grids than the one used in the present simulations. Table 3 summarizes the numerical resolutions in the various numerical simulations.

10. Heat transfer on the back surface

The local Nusselt number is quite variable both in time and space. At high Reynolds numbers, the heat-transfer rate on the back surface can become greater than the FSP

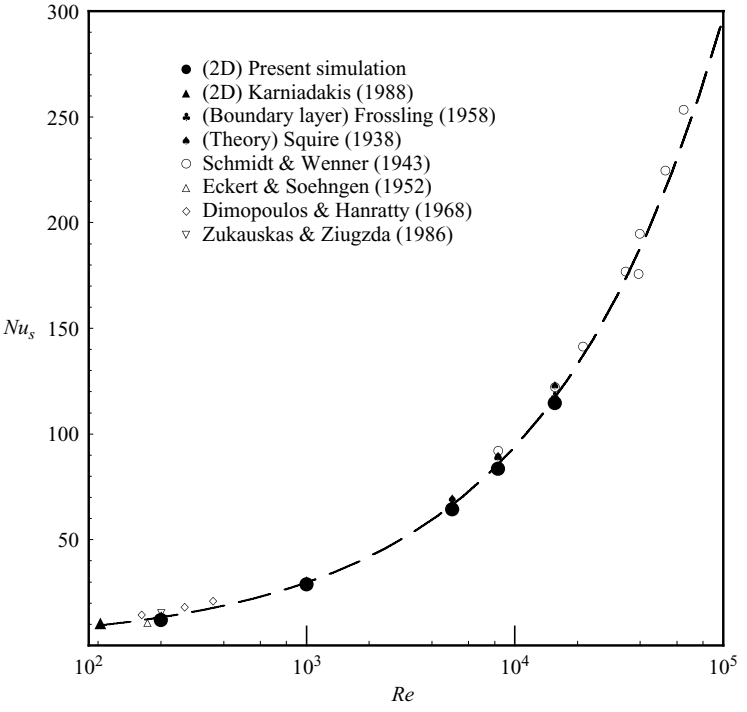

FIGURE 14. Nusselt number at the front stagnation point, Nu_s, as a function of the Reynolds number Re. The solid symbols denote the numerical results and the open symbols the experimental data. The dashed line is (9.1).

value. As shown in figure 13(c) for $Re = 15\,550$, one maximum on the back surface is $Nu = 190$, which is 65 % higher than the FSP value of $Nu_s = 115$, at time $t = 100$. The heat transfer on the back surface is highly unsteady; however, the available experimental data are based on time-averaged measurements. Figure 15 shows the time-averaged Nu profiles obtained from the present simulations for two Reynolds numbers, $Re = 1000$ and 5000. The figure also shows the first pair of minima in these profiles due to the initial separation of the boundary layer. The angular positions of this first pair of minima, $\theta_{Nu_{min}}$, obtained from the simulations, are shown, together with the experimental data for comparison in figure 16. These minima move back and forth over a range of angular displacement, as thermal energy is released in an unsteady manner from the surface of the cylinder. The vertical lines passing through the solid symbols in the figure define the range of these movements. The $\theta_{Nu_{min}}$ data in figure 16 follow a similar trend to the data for θ_s in figure 5. However, the angle $\theta_{Nu_{min}}$ is greater than θ_s because the flares are located on the downstream side of the flow separations.

Eckert & Soehngen (1952) and Schmidt & Wenner (1943) measured the local distribution of the heat-transfer coefficient around the cylinder circumference. Their data are given in figures 17(a)–(c) and may be compared with the time-averaged profiles obtained from the present simulation for $Re = 200$, 8290 and 15 550, respectively. The pattern obtained from the present simulation is reasonably aligned with the observations at $Re = 200$. It is not in perfect agreement with the experimental data at the higher Reynolds numbers. This discrepancy between the simulations and experiments could be due to the disturbances produced by the instrumentation panel

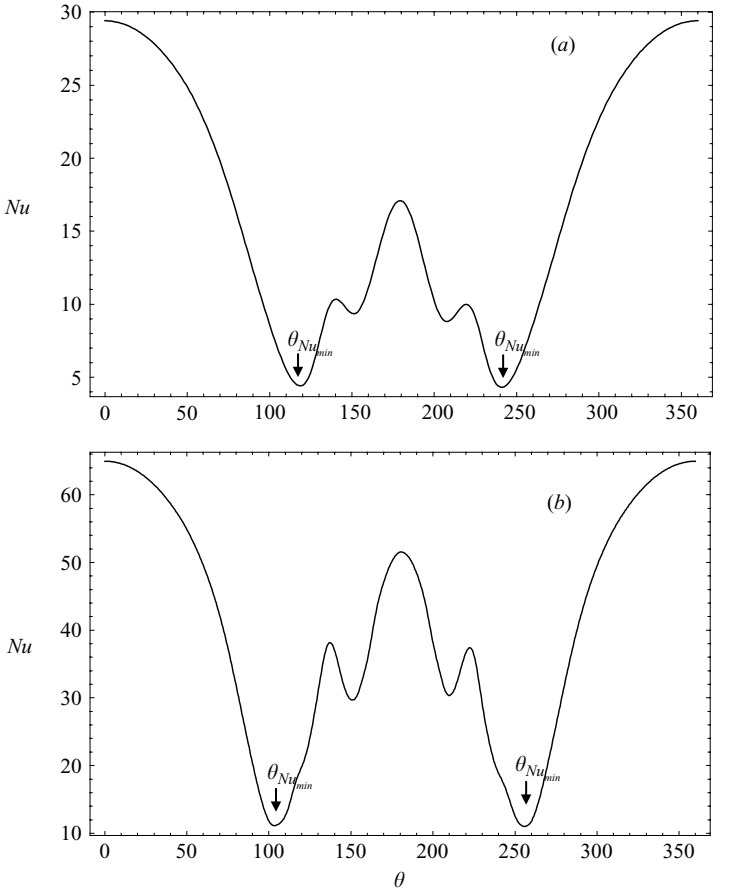

FIGURE 15. Time-averaged Nusselt number obtained over a period of time from $t = 30$ to $t = 100$ for two Reynolds numbers, (*a*) $Re = 1000$ and (*b*) $Re = 5000$.

in Schmidt & Wenner's (1943) experiment, resulting in their admitted measuring error. The discrepancy could also be partly explained by the buoyancy effect and by three-dimensional motions, which have been ignored in the present simulation. The cylinder in Schmidt and Wenner's experiment was oriented with its axis in the vertical direction. The flow induced by buoyancy may have disturbed the boundary layer, and that could explain the higher FSP heat-transfer rate and the earlier boundary-layer separation in the experiment. Despite the discrepancy, the general pattern of the simulation profiles is consistent with the experimental observation. The most remarkable features of the simulated profiles are the sharp peaks that occur immediately downstream of the initial separation, as marked by the arrows in figure 17. These peaks were not detected by Schmidt & Wenner (1943) at the present Reynolds numbers of $Re = 8239$ and 15 550 but were observed in their experiments at higher Reynolds numbers. According to the measurements by Schmidt and Wenner at higher Reynolds numbers, the Nusselt numbers at the sharp peaks are $Nu_{sp} = 448$, 660 and 1377 for $Re = 170\,000$, 257 000 and 426 000, respectively. These peak values on the back surface, obtained from the time-average profiles, may be compared with the respective values $Nu_s = 443$, 500 and 716 at the FSP. The peak values on the back surface are high compared with the values on the FSP despite the smoothing effect

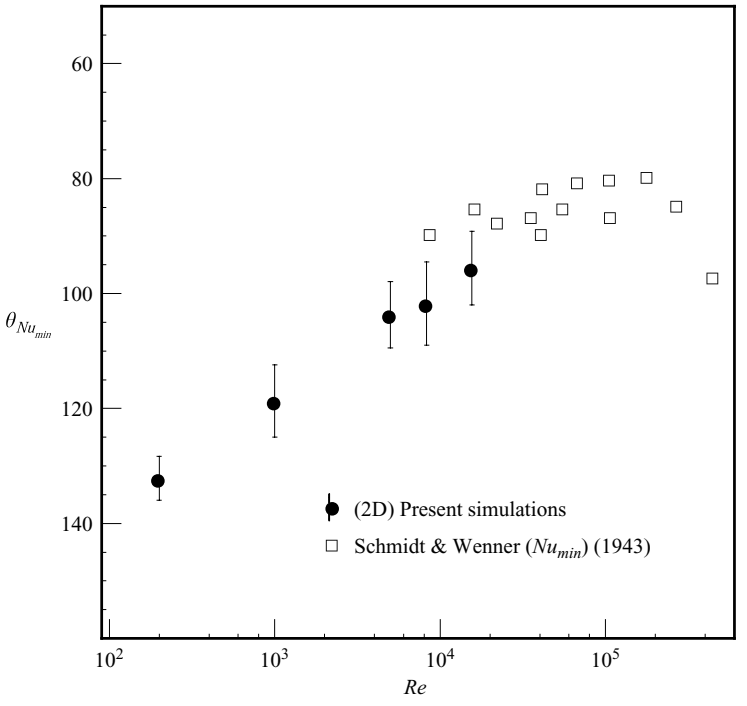

FIGURE 16. Separation angles based on the first pair of Nu minima. The open symbols denote the results obtained from laboratory measurements by Schmidt & Wenner (1943). The solid symbols denote the location of the heat-transfer minimum obtained from the numerical simulation.

of the time averaging. The intensity of the peaks becomes still higher with increasing Reynolds number. This trend is correctly predicted by the two-dimensional models.

11. Circumferential and overall averages

The circumferential average $\tilde{Nu}$ is obtained by integrating the local Nu over the surface of the cylinder:

$$\tilde{Nu} = \frac{1}{2\pi}\int_0^{2\pi} Nu(\theta)\,\mathrm{d}\theta. \tag{11.1}$$

Owing to the wake oscillation, this circumferential average $\tilde{Nu}$ is a function of time. The variations in $\tilde{Nu}$ with time is shown in panel (c) of each of figures 6–9, for $Re = 100$, 5000, 8290 and 15 550, respectively. The averaging of these circumferential averages over time, from $t = 30$ to 100, gives the overall averages $\overline{Nu} = (t_2 - t_1)^{-1} \int_{t_1=30}^{t_2=100} \tilde{Nu}\,\mathrm{d}t$. The results of the present simulations are as follows: $\overline{Nu} = 6.55$, 14.7, 37.7, 51.4 and 74.8 for $Re = 200$, 1000, 5000, 8290 and 15 550, respectively. Most experiments in the past were conducted to measure this overall $\overline{Nu}$. The data are summarized in table 4 and plotted in figure 18. Also included in the figure, for comparison, is the following relation, recommended by Eckert & Drake (1972) on the basis of the experimental data:

$$\overline{Nu} = (0.43 + 0.5Re^{0.5})Pr^{0.38} \tag{11.2}$$

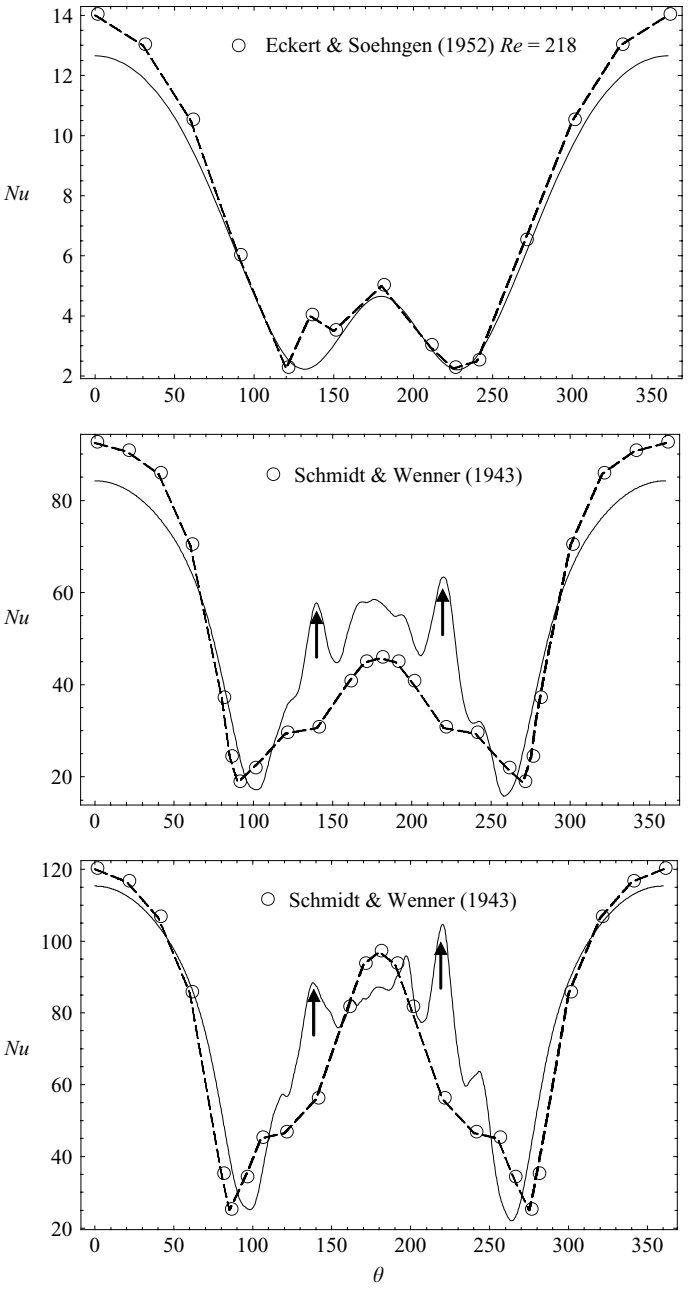

FIGURE 17. Time-averaged Nusselt number obtained over the period $t = 30$ to $t = 100$ for $Re = 200$, 8290 and 15 550 with experimental data of Eckert & Soehngen (1952) and Schmidt & Wenner (1943) for comparison.

for $1 < Re < 10^3$ and

$$\overline{Nu} = 0.25 Re^{0.6} Pr^{0.38} \tag{11.3}$$

for $10^3 < Re < 10^5$. The $\overline{Nu}$ obtained from the present two-dimensional simulations covers a much wider range of Reynolds numbers than any previous simulation.

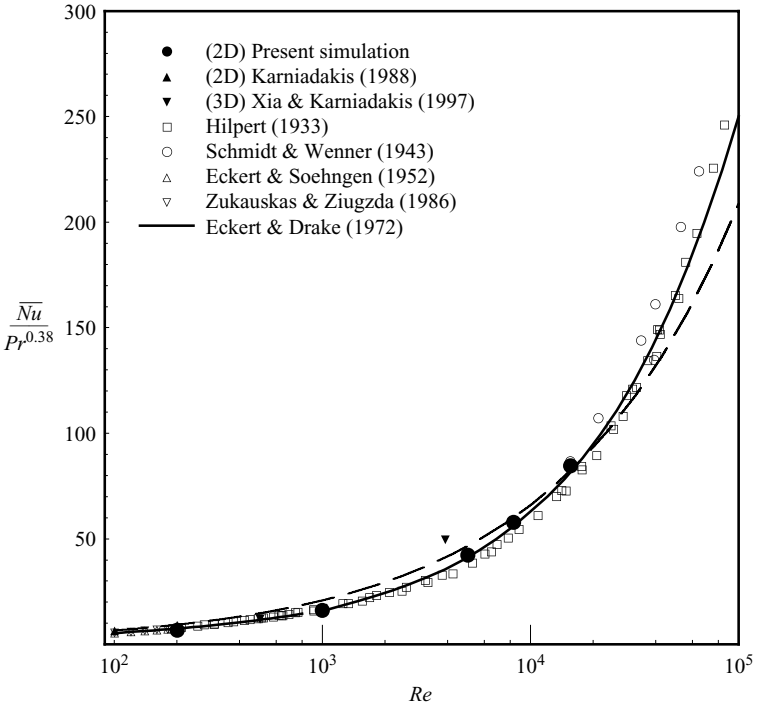

FIGURE 18. Overall average Nusselt number $\overline{Nu}$ as a function of the Reynolds number. The solid line is the formula of Eckert & Drake (1972) filled to the experimental data. The dashed line is (11.4).

Despite the possibility of three-dimensional effects, the two-dimensional results are in excellent agreement with the experimental data. They even appear to be in better agreement than one of the three-dimensional simulation results for $Re = 3900$ obtained by Xia & Karniadakis (1997). These authors conducted their simulations using a finite-element mesh of 400 elements. The size of their mesh at the wall is unknown and may not have been sufficiently small to resolve the steep-wall temperature and velocity gradients at Reynolds number $Re = 3900$.

For the narrow range of Reynolds numbers in the present simulations, the overall Nusselt number fits the formula

$$\overline{Nu} = 0.66 Re^{0.5} Pr^{0.38}, \tag{11.4}$$

which is shown as a dashed line in figure 18. This dependence on Reynolds number to the power one-half suggests an overall thermal-boundary-layer thickness in proportion to δ_1,

$$\overline{\delta}_T \simeq 5.2\delta_1. \tag{11.5}$$

However, if the Nusselt number depended on Reynolds number according to the formula of Eckert & Drake (1972), the thermal-boundary-layer thickness would depend on the Reynolds number as follows:

$$\left.\begin{aligned} \overline{\delta}_T &= 5.2\delta_1 \quad \text{for} \quad Pr = 0.7 \text{ and } Re = 1000, \\ \overline{\delta}_T &= 4.1\delta_1 \quad \text{for} \quad Pr = 0.7 \text{ and } Re = 10\,000. \\ \overline{\delta}_T &= 3.3\delta_1 \quad \text{for} \quad Pr = 0.7 \text{ and } Re = 100\,000. \end{aligned}\right\} \tag{11.6}$$

Over the wider range of Reynolds numbers from $Re = 1000$ to 10 000, the overall thermal-boundary-layer thickness decreases slightly from $\bar{\delta}_T = 5.2\delta_1$ to $3.3\delta_1$. These thicknesses of the thermal boundary layer are of the same order of magnitude as the flare thickness, which is estimated to be equal to $7\delta_1$ (see figure 3). The thermal-boundary-layer thickness at the FSP is fixed at $(\delta_T)_s = 3.25\delta_1$, (9.3). The overall thickness tends to decrease with the Reynolds number and is thinner than the FSP thickness if the Reynolds number is greater than $Re = 100\,000$. This reduction in overall thickness with Reynolds number suggests that the thermal boundary layer on the back surface can actually become thinner than the layer at the FSP, if the Reynolds number is sufficiently high.

12. Back-to-total heat-transfer ratio

The proportion of thermal energy released from the back side of the cylinder is obtained by integration over the back surface. The demarcation between the front and the back is defined by angles θ_1 and θ_2, which are the angles associated with the first pair of Nusselt-number minima in the time-averaged profile $\tilde{Nu}(\theta)$. With this definition of the demarcation angle, the fraction of heat released from the back relative to the total heat released is

$$R = \frac{\dfrac{1}{2\pi}\displaystyle\int_{\theta_1}^{\theta_2} \tilde{Nu}(\theta)\,\mathrm{d}\theta}{\dfrac{1}{2\pi}\displaystyle\int_{0}^{2\pi} \tilde{Nu}(\theta)\,\mathrm{d}\theta}. \tag{12.1}$$

Table 4 gives the value of this ratio. At the low Reynolds number of $Re = 200$, only $R = 13.2\,\%$ of the heat is released from the back side of the cylinder. The ratio increases to 40.5 % at $Re = 15\,550$. Figure 19 shows how this ratio R varies with the Reynolds number. The results of the simulations follow closely the trend of the experimental data obtained by Schmidt & Wenner (1943). The proportion of the heat flux coming from the back continuously increases with Reynolds number. The high heat-transfer rate on the back is consistent with the instantaneous profiles of Nu shown in figure 13. For $Re = 15\,550$, the instantaneous peak heat-transfer rate on the back side of the cylinder is 65 % higher than the value at the front stagnation point, as shown in figure 13(*c*). This high instantaneous rate is associated with the steep temperature gradient that occurs within a very thin viscous layer at this location and time.

The present two-dimensional results for the back-to-total heat transfer ratio are approximately 10 % higher than the data of Schmidt & Wenner (1943). These high two-dimensional results are probably due to the absence of three-dimensional structures in the two-dimensional model. The three-dimensional structure may thicken the viscous layer and hence lower the heat-transfer rate from the back surface of the cylinder.

13. Viscous and thermal layers on the back surface

After the initial flow separation, there remain thin viscous layers on the back surface of the cylinder. The existence of such viscous layers is shown in figure 20 by the two components of the velocity, v_r and v_θ, in the vicinity of the wall. The thick lines in the figure denote the profile of the velocity components within the immediate vicinity of the wall, i.e. at $r = a + (\Delta r)_1$. The thin lines denote components at eight computational

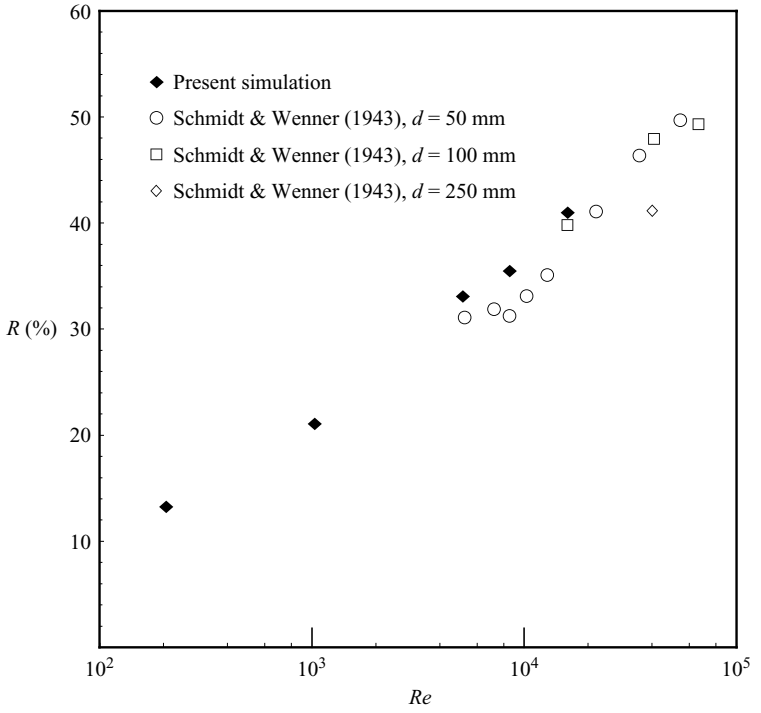

FIGURE 19. Proportion of the heat transfer over the back of the cylinder. The computation results are compared with the experimental data obtained by Schmidt and Wenner (1943).

cells away from the wall, i.e. $r = a + \sum_{i=1}^{8} (\Delta r)_i$. The tangential component v_θ increases rapidly, becoming significantly greater than the radial component v_r over a very short distance from the wall. The radial component v_r stays small except in regions close to the flares. Figure 21 shows the tangential-velocity profiles for two locations. The thin line is the v_θ-profile on the side of the cylinder where $\theta = 60°$. The thick line corresponds to the velocity profile at one location on the back of the cylinder at $\theta = 210°$, where the Nusselt number is a local maximum. The thickness of the viscous layer at this location on the back surface is actually less than that of the boundary layer on the side. The thinness of the viscous layer is responsible for the high heat-transfer rate at this location, where $\theta = 203°$, as shown in figure 13(*c*).

The viscous layers and flares are necessary elements to explain the observed high heat-transfer rate from the back surface of the cylinder. Release of thermal energy from the back surface by conduction requires a high thermal gradient that can only be found in thin viscous layers. The rate of heat conduction is inversely proportional to the thickness of a viscous layer. The higher the Reynolds number, the thinner the viscous layer and therefore greater the heat transfer from the surface of the cylinder to the viscous layer. At high Reynolds number, the thermal energy trapped in the layer is released from it first by convection to the flares and subsequently through the flares into the wake. This concept of thermal-energy release from the back surface of the cylinder shows the complementary role between convection and conduction, and the side-by-side existence of flares and viscous layers. The concept would not be feasible if one existed without the other.

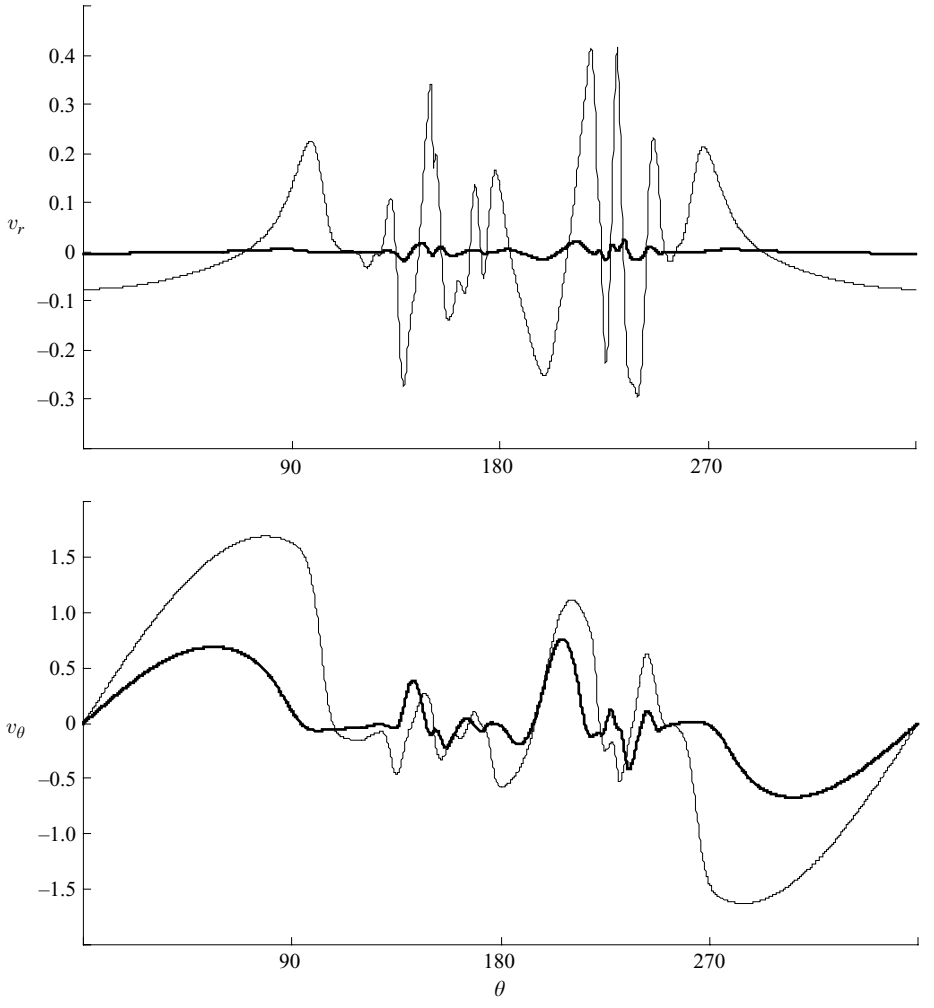

FIGURE 20. Radial component v_r and tangential component v_θ of the velocity in regions close to the wall at time $t = 100$ and $Re = 15\,550$.

At Prandtl number $Pr = 0.7$, the viscous layers and the thermal layers are comparable in thickness and both are proportional to the viscous length scale δ_1, which in turn is inversely proportional to $Re^{1/2}$. The thermal energy is a passive tracer that does not impact on the flow. The thickness of the thermal boundary layer may change with the Prandtl number. The overall structures of the viscous layers and the flares depend only on the Reynolds number. The relation between flares and eddies will be explained further in subsequent sections.

14. Flares and eddies

The maxima and minima of the *Nu* profiles define the thermal structure on the surface of the cylinder. The maxima flow towards the wall ($v_r < 0$), while the minima flow away from the wall ($v_r > 0$). The thermal energy is confined within and is advected along the viscous layers. The flares release the thermal energy from the viscous layers by directing it away from the wall. The viscous layers and the flares on the surface

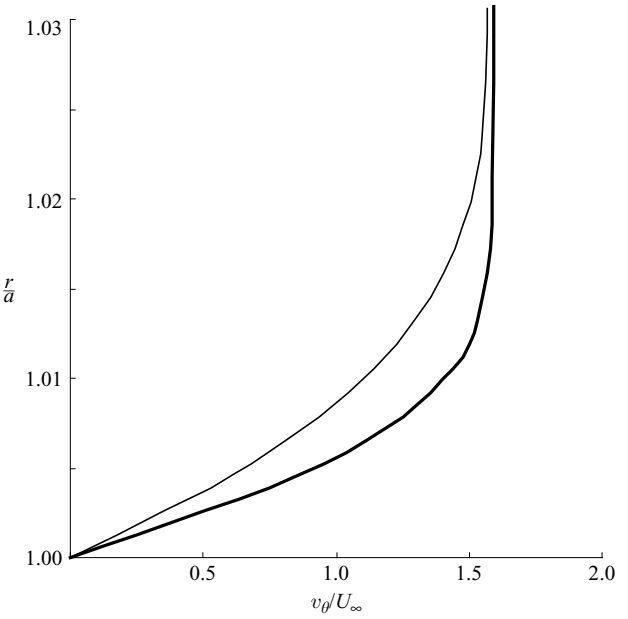

FIGURE 21. Tangential velocity profile on the side where $\theta = 60°$, denoted by the thin line and the profile on the back where $\theta = 210°$, denoted by the thick line at the instant of time $t = 100$ for Reynolds number $Re = 15\,550$.

of the cylinder occur at the maxima and minima of the $Nu(\theta)$ profiles. Panels (b) of figures 6–9 show the loci of these maxima and minima for $Re = 1000$, 5000 and 15 550, respectively. The maxima and the minima trace lines over space and time in these figures. At a given instant, the traces alternate between maxima and minima along the cylinder wall and are enveloped by two outermost minima traces. The population numbers of these maxima plus the minima, n_{Nu}, were obtained from the loci at each instant and are plotted versus time in figure 22(a). In a similar manner, the number of zeros associated with the tangential-velocity gradient, $n_{\partial_\theta v_\theta}$, and the number of zeros associated with the radial velocity component, n_{v_r}, are plotted in figure 22(b), (c) for comparison with the n_{Nu} plot in figure 22(a). All three numbers, n_{Nu}, $n_{\partial_\theta v_\theta}$ and n_{v_r}, follow similar variations with time. The time-averaged values of these numbers at $Re = 15\,550$, over the period $t = 30$ to 100, are $\overline{n}_{Nu} = 23.5$, $\overline{n}_{\partial_\theta v_\theta} = 24.3$, and $\overline{n}_{v_r} = 24.9$. All three averages have similar dependences on the Reynolds number, confirming the association of the flares with the zeros of $\partial_\theta v_\theta$ and the zeros of v_r. The flares do not occur at locations where $\partial v_\theta/\partial\theta = 0$ and $v_r = 0$ but are located in regions between these zeros.

Since flow separations are defined by the vorticity zeros, that is at locations where $\partial v_\theta/\partial r = 0$, it can be shown that the flares do not occur at the same location as these vorticity zeros. The tangential gradient of the tangential velocity $\partial v_\theta/\partial\theta$ determines the direction of the radial component of the velocity, v_r. A thin boundary layer forms at locations where the radial component of the velocity v_r is directed toward the wall. The flares of thermal energy occur at locations where the radial velocity is directed away from the wall ($v_r > 0$). These locations are also the locations where $\partial v_\theta/\partial\theta < 0$, according to the continuity equation

$$\frac{v_r}{r} + \frac{\partial v_r}{\partial r} + \frac{1}{r}\frac{\partial v_\theta}{\partial\theta} = 0, \tag{14.1}$$

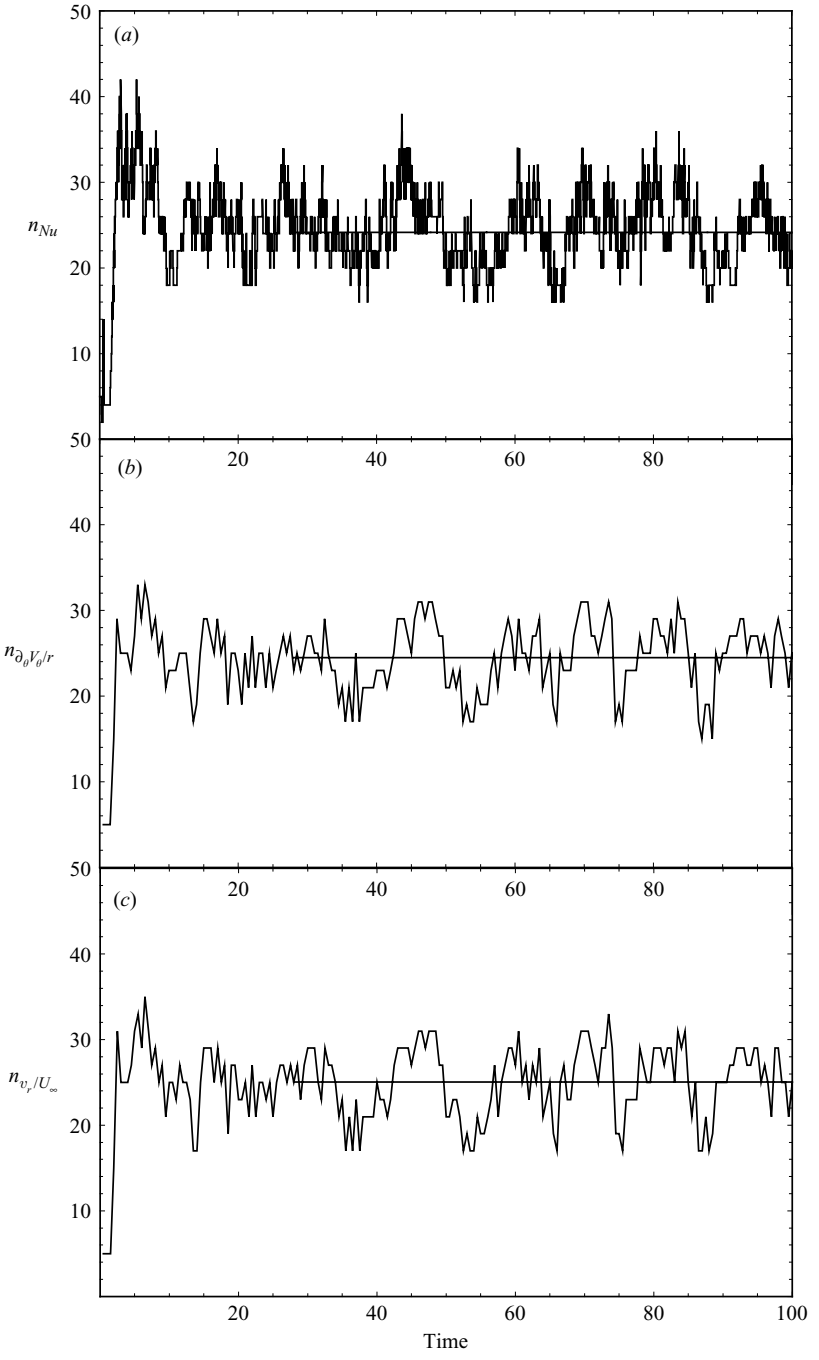

FIGURE 22. (*a*) The number of *Nu* maxima plus *Nu* minima, (*b*) the number of v_θ-gradient zeros and (*c*) the number of v_r zeros at $Re = 15\,550$. The average numbers of maxima plus minima over the period from $t = 30$ to 100 are $\overline{n}_{Nu} = 23.5$ and $\overline{n}_{\partial_\theta v_\theta} = 24.3$ for $Re = 15\,550$.

since in regions close to the wall the term $\partial v_r/\partial r$ is negligibly small; therefore

$$v_r \simeq -\frac{\partial v_\theta}{\partial \theta}. \tag{14.2}$$

According to this relation, a negative tangential gradient $\partial v_\theta/\partial\theta$ is associated with a positive v_r, which directs the flare of heat away from the wall. However, the viscous layer is associated with a positive tangential gradient, $\partial v_\theta/\partial\theta > 0$, and the direction of v_r toward the wall.

The data obtained for the number of *Nu* maxima plus the minima, $\overline{n}_{Nu}$, are plotted versus the Reynolds number in figure 12(*a*). The data in the figure fit the relation

$$\overline{n}_{Nu} \simeq 0.191\sqrt{Re}. \tag{14.3}$$

The population number of the flares is equal to one-half of this, i.e.

$$\overline{n}_F = \tfrac{1}{2}\overline{n}_{Nu} \simeq 0.0953\sqrt{Re}, \tag{14.4}$$

because the flares are associated only with the *Nu* minima. The average spacing between the flares, λ_F, is the arclength πa divided by the number of flares, i.e.

$$\lambda_F = \frac{\pi a}{\overline{n}_F} = \frac{\pi}{0.0953 \times 0.67}\frac{0.67a}{\sqrt{Re}} \simeq 49.6\delta_1. \tag{14.5}$$

According to this formula, the spacing between the flares is

$$\lambda_F \simeq 50\delta_1, \tag{14.6}$$

which is comparable with the average spacing of eddies, $\lambda_E \simeq 44\delta_1$, (7.2). The average spacing between the eddies and flares may be compared with the width of the flares, $w \simeq 7\delta_1$, (5.1). The FSP displacement thickness δ_1 is a viscous length scale. The eddy and flare spacings, λ_E and λ_F, and the flare width w are in proportion to this viscous length scale.

The number n_{Nu} changes with time by 2 each time a flare is created or detached from the back surface. The frequency of detachment of the flares is f_F. The dimensionless parameter associated with the flare-detachment frequency is the flare Strouhal number $St_F = f_F D/U_\infty$, which follows an approximately linear relation with the Reynolds number,

$$St_F = \frac{f_F D}{U_\infty} \simeq 0.00065Re, \tag{14.7}$$

as shown in figure 12(*b*). This relation for the flare Strouhal number follows essentially the same functional relation as the eddy Strouhal number St_E, discussed in § 7. Although the locations of the flares do not coincide with the vorticity zeros, the population number of the flares and the number of the eddies are essentially the same: $\overline{n}_F \simeq \overline{n}_E$. The flare-detachment and eddy-detachment frequencies are also the same: $St_F \simeq St_E$ and $f_F\nu/U_\infty^2 \simeq f_E\nu/U_\infty^2 \simeq 0.00065$–$0.00074$.

Table 5 summarizes the results obtained from the present simulations. The table also includes calculation results for $Re = 1000$, repeated with a coarser grid and with a finer grid. The effect of these grid changes is almost negligible, although the flare Strouhal number St_F is slightly affected. It should be noted that (7.1), (7.3), (14.4) and (14.7) are tentative asymptotic relations derived from a small data set. The form and the constants in these equations may have to be modified when more data are obtained from future simulations of the flow at higher Reynolds numbers.

15. Summary and conclusions

The heat transfer from a circular cylinder into a crossflow is first by heat conduction in the viscous layer on the back surface of the cylinder. The subsequent release of heat

Re	Grid	$(\Delta r)_1$	θ_s	θ_{Nu}	$\overline{Nu}$	Nu_s	R	St	$\overline{n}_E$	$\overline{n}_F$	St_E	St_F
200	70×140	δ_1	$111° \pm 2°$	$132° \pm 4°$	6.55	12.7	13.2	0.190	4.09	2.00	0.36	0.00
1000	75×150	$2\delta_1$	$102° \pm 9°$	$120° \pm 5°$	14.7	26.8	20.5	0.232	6.46	4.54	1.50	0.91
	150×300	δ_1	$102° \pm 8°$	$119° \pm 6.5°$	14.7	26.5	21.0	0.224	6.52	3.39	1.54	0.48
	300×600	$\frac{1}{2}\delta_1$	$103° \pm 8°$	$119° \pm 4°$	14.6	26.4	21.3	0.222	6.52	3.40	1.58	0.42
5000	340×680	δ_1	$90.0° \pm 6°$	$104° \pm 5.5°$	37.7	65.0	31.1	0.228	8.86	6.40	3.25	2.17
8290	430×860	δ_1	$92.5° \pm 9.5°$	$102° \pm 7.5°$	51.4	84.2	34.8	0.224	10.1	8.43	6.47	4.87
15 550	600×1200	δ_1	$86.5° \pm 6.5°$	$95.5° \pm 6.5°$	74.8	115	40.5	0.210	14.0	12.1	11.3	10.8

TABLE 5. Summary of numerical results of the present simulations. Notes $a(\Delta\theta)_1 = (\Delta r)_1$.

into the wake is due to the detachment of eddies and flares from the back surface. In the present simulations, these heat-transfer processes were computed using a two-dimensional model for Reynolds numbers $Re = 200$, 1000, 5000, 8290 and 15 550 and Prandtl number $Pr = 0.7$. The mesh size was refined in proportion to a viscous length scale δ_1, to ensure uniform accuracy of the calculations for all Reynolds numbers. The results of the simulations using the refined grid show that the local heat transfer on the surface of the cylinder is highly variable in space and time. The heat-transfer rate on the back surface can be at times significantly greater than the rate at the front stagnation point. This high and localized heat-transfer rate is associated with the formation of thin viscous layers on the back surface of the cylinder. The release of vorticity and the release of thermal energy from these viscous layers by eddies and flares are unsteady processes characterized by two sets of scales. The initial separation of the boundary layer is characterized by the Strouhal number $St = f D/U_\infty$, which is proportional to the diameter of the cylinder. The local release of vorticity and thermal energy is characterized by eddies and flares of significantly higher frequencies, such that $f_F \nu/U_\infty^2 \simeq f_E \nu/U_\infty^2 \simeq 0.00065$–$0.00074$, which are related to the viscous time scale ν/U_∞^2. At high Reynolds numbers, these eddy and flare frequencies are independent of the diameter of the cylinder. The heat flares have an average spacing $\lambda_F \simeq 49\delta_1$ and a width $w \simeq 7\delta_1$. The thermal-boundary-layer thickness at the front stagnation point is equal to $(\delta_T)_s \simeq 3.25\delta_1$. However, a greater proportion of the thermal energy is released from the back with increased Reynolds number. The overall thickness of the thermal boundary layer decreases with Reynolds number from $\overline{\delta_T} \simeq 5\delta_1$ at $Re = 200$ to $\overline{\delta_T} \simeq 3\delta_1$ at $Re = 15\,550$. The back-to-total heat-transfer ratio R increases from 13 % at $Re = 200$ to 41 % at $Re = 15\,550$. This continuous increase of R with Reynolds number is simulated by the two-dimensional model, in agreement with experimental observations.

The two-dimensional model is an approximation to the three-dimensional reality. Given finite computational resources, the trade-off is between two-dimensional calculations for high Reynolds numbers and three-dimensional computations at lower Reynolds numbers. Two-dimensional simulations, although constrained, can in some cases give important physical insight, whereas in other cases they can be misleading. With some exceptions, the two-dimensional model closely simulates the trend of the dependences a number of flow parameters on Reynolds number. The angles of flow separations θ_s and $\theta_{Nu_{min}}$, shown in figures 5 and 16, are examples of this trend. There are some differences. The most notable difference occurs at $Re = 8290$, where $\theta_s = 92.5° \pm 9.5°$ and $\theta_{Nu_{min}} = 101.5° \pm 7.5°$ in the two-dimensional model, which may be compared with $\theta_s \simeq 85°$ and $\theta_{Nu_{min}} \simeq 90°$ by experiment (respectively).

Another example is the Strouhal number in figure 10. Starting from $Re = 190$–260 in the wake transition regime, the two-dimensional model consistently overestimates the Strouhal number (Williamson 1996). At $Re = 8290$, the Strouhal number is $St = 0.224$ in the model and $St \simeq 0.195 \sim 0.22$ by experiment. There is a more complex dependence of the drag coefficient on Reynolds number. The drag coefficient is slightly underestimated by the two-dimensional model in the range of Reynolds numbers from $Re = 40$ to 200 but slightly overestimated in the range from $Re = 200$ to 5000 (Kawaguti & Jain 1966; Jordan & Fromm 1972; Collins & Dennis 1973; Bouhairie 2005). Beyond these ranges of Reynolds numbers, Singh & Mittal (2004) captured the drag crisis using a two-dimensional model at Reynolds number $\mathrm{Re} \simeq 2 \times 10^5$, despite the presence of three-dimensional structures at those Reynolds numbers. The fluctuating lift is the flow parameter that is the most sensitive to the presence of three-dimensional flow structures. Out-of-phase vortex shedding can lead to cancellation of the lift forces along the span and therefore to a reduction in the root-mean-square value of the fluctuating lift (Norberg 2003). Although two-dimensional calculations significantly overestimate the fluctuating lift, many existing high-Reynolds-number vortex-induced vibration studies have been based on two-dimensional or quasi-two-dimensional models and so it has been possible to produce qualitative agreement with experiment using these models (Mittal & Balachandar 1995; Henderson 1998; Al-Jamal & Dalton 2004; Willden & Graham 2004).

The heat-transfer parameters are less susceptible to three-dimensional variations in the spanwise direction, for the range of Reynolds number considered. The present two-dimensional simulations, using the refined grid giving uniform accuracy for all Reynolds numbers, have closely captured the front-stagnation heat-transfer rate (figure 14), the overall heat-transfer rate (figure 18) and the observed trend of the high heat-transfer rate from the back surface of the cylinder at high Reynolds number (figure 19). The two-dimensional simulations also resolved the viscous layers on the back surface and the side-by-side existence of the flares as necessary mechanisms for a high heat-transfer rate on the back surface of the cylinder. Without a doubt, there are disparities between the results of the two-dimensional and three-dimensional computations. However, accurate and systematic analyses of the two-dimensional results, as presented in this paper, are necessary to facilitate future simulations and measurements of two-dimensional and three-dimensional heat-transfer processes at still higher Reynolds numbers.

REFERENCES

Adachi, T., Okamoto, S. & Adachi, M. 1979 The effect of sound on the rate of heat transfer from a cylinder placed normal to an air stream. *Bulletin JSME* **22**, 1407–1415.

Al-Jamal, H. & Dalton, C. 2004 Vortex induced vibrations using large eddy simulation at moderate reynolds number. *J. Fluids Struct.* **19**, 73–92.

Behr, M. 1992 Stabilized finite element methods for incompressible flows with emphasis on moving boundaries and interfaces. PhD thesis, University of Minnesota, Minnesota.

Behr, M., Hastreiter, D., Mittal, S. & Tezduyar, T. E. 1995 Incompressible flow past a circular cylinder: Dependence of the computed flow field on the location of the lateral boundaries. *Comput. Meth. Appl. Mech. Engng* **123**, 309–316.

Behr, M., Johnson, A., Kennedy, J., Mittal, S. & Tezduyar, T. E. 1993 Computation of incompressible flows with implicit finite element implementations on the connection machine. *Comput. Meth. Appl. Mech. Engng* **108**, 99–118.

Behr, M., Liou, J., Shih, R. & Tezduyar, T. E. 1991 Vorticity-streamfunction formulation of unsteady incompressible flow past a cylinder: sensitivity of the computed flow field to the location of the outflow boundary. *Intl J. Num. Meth. Fluids* **12**, 323–342.

Bouhairie, S. 2005 Computational methods for calculating heat transfer from a circular cylinder in a cross flow. PhD thesis, McGill University, Montreal, Quebec, Canada.

Braza, M., Chassaing, P. & Minh, H. H. 1986 Numerical study and physical analysis of the pressure and velocity fields in the near wake of a circular cylinder. *J. Fluid Mech.* **165**, 79–130.

Chou, M. H. & Huang, W. 1996 Numerical study of high-reynolds-number flow past a bluff object. *Intl J. Num. Meth. Fluids* **23**, 711–723.

Collins, W. M. & Dennis, S. C. R. 1973*a* The initial flow past an impulsively started circular cylinder. *Q. J. Mech. Appl. Maths* **26** (1), 53–75.

Collins, W. M. & Dennis, S. C. R. 1973*b* Flow past an impulsively started circular cylinder. *J. Fluid Mech.* **60**, 105–127.

Coutanceau, M. & Bouard, R. 1979 Mécanique des fluides – sur la formation de tourbillons $\ll$ *secondaires* $\gg$ dans le sillage d'un cylindre soumis à un départ impulsif. *C. R. Acad. Sci. Paris* **288** B, 45–60.

Coutanceau, M. & Defaye, J. 1991 Circular cylinder wake configurations: a flow visualisation survey. *Appl. Mech. Rev.* **44**, 255–305.

Daube, O. & Ta Phouc Loc 1978 Étude numérique d'écoulements instationnaires de fluide visqueux incompressible autour de corps profiles par une méthode combinée d'ordre $0(h^2)$ et $0(h^4)$. *J. Méc.* **17**, 651–678.

Dennis, S. C. R. & Chang, G.-Z. 1969 Numerical integration of the navier-stokes equations for steady two-dimensional flow. *Phys. Fluids Suppl.* II **12**, 88–93.

Dennis, S. C. R. & Chang, G.-Z. 1970 Numerical solutions for steady flow past a circular cylinder at reynolds numbers up to 100. *J. Fluid Mech.* **42**, 471–489.

Dennis, S. C. R., Hudson, J. D. & Smith, N. 1968 Steady laminar forced convection from a circular cylinder at low reynolds numbers. *Phys. Fluids* **11**, 933–940.

Dennis, S. C. R. & Staniforth, A. N. 1971 A numerical method for calculating the initial flow past a cylinder in a viscous fluid. In *Proc. 2nd Intl Conf. Num. Meth. Fluid Dyn., Lect. Notes Phys.*, vol. 8, pp. 343–349. Springer.

Dimopoulos, H. G. & Hanratty, T. J. 1968 Velocity gradients at the wall for flow around a cylinder for reynolds numbers between 60 and 360. *J. Fluid Mech.* **33**, 303–319.

Dong, S. & Karniadakis, G. E. 2005 Dns of flow past a stationary and oscillating cylinder at $Re = 10000$. *J. Fluids Struct.* **20**, 519–531.

Eckert, E. R. G. & Drake, R. M. 1972 *Analysis of Heat and Mass Transfer*. McGraw-Hill.

Eckert, E. R. G. & Soehngen, E. 1952 Distributions of heat transfer coefficients around circular cylinders in crossflow at reynolds numbers from 20 to 500. *Trans. ASME* **75**, 343–347.

Engelman, M. S. & Jamnia, M. A. 1990 Transient flow past a circular cylinder: a benchmark solution. *Intl J. Num. Meth. Fluids* **11**, 985–1000.

Evangelinos, C. & Karniadakis, G. E. 1999 Dynamics and flow structures in the turbulent wake of rigid and flexible cylinders subject to vortex-induced vibrations. *J. Fluid Mech.* **400**, 91–124.

Fage, A. & Falkner, V. M. 1931 Further experiments on the flow around a circular cylinder. *Tech. Rep.* 1369. Aero. Res. Ctee.

Frossling, N. 1958 Evaporation, heat transfer and velocity distribution in two-dimensional and rotationally symmetrical laminar boundary-layer flow. *Tech. Rep.* 1432. Nat. Advisory Ctee Aero.

Grove, A. S., Shair, F. H., Peterson, E. E. & Acrivos, A. 1964 An experimental investigation of the steady separated flow past a circular cylinder. *J. Fluid Mech.* **19**, 60–85.

Hatanaka, K. & Kawahara, M. 1995 A numerical study of vortex shedding around a heated/cooled circular cylinder by the three-step taylor-galerkin method. *Intl J. Num. Meth. Fluids* **21**, 857–867.

Hayase, T., Humphrey, J. A. C. & Greif, R. 1992 A consistently formulated quick scheme for fast and stable convergence using finite-volume iterative calculation procedures. *J. Comp. Phys.* **98**, 108–118.

Henderson, R. D. 1997 Nonlinear dynamics and pattern formation in turbulent wake transition. *J. Fluid Mech.* **352**, 65–112.

Henderson, R. D. 1998 Turbulent wake transition. In *Advances in the Understanding of Bluff Body Wakes and Vortex-Induced Vibrations* (ed. P. W. Bearman & C. H. K. Williamson). ASME.

Henderson, R. D. & Karniadakis, G. E. 1995 Unstructured spectral element methods for simulation of turbulent flows. *J. Comp. Phys.* **122**, 191–217.

Hiemenz, K. 1911 Die grenzschicht an einem in den gleichformigen flussigkeitsstrom eingetauchten geraden kreiszylinder. thesis, gottingen. *Dingl. Polytechn. J.* **326**, 321.

Hilpert, R. 1933 Wärmeabgabe von geheizten drähten und rohren im luftstrom. *Forschung Auf Dem Gebiete Des Ingenieurwesens* **4**, 215–224.

Holman, J. P. 1990 *Heat Transfer*, 7th edn. McGraw-Hill.

Jain, P. C. & Rao, K. S. 1969 Numerical solution of unsteady viscous incompressible fluid flow past a circular cylinder. *Phys. Fluids Supp.* II **12**, 57–64.

Jordan, S. A. & Ragab, S. A. 1998 A large-eddy simulation of the near wake of a circular cylinder. *Trans. ASME: J. Fluids Engng* **120**, 243–252.

Jordan, S. K. & Fromm, J. E. 1972 Oscillatory drag, lift, and torque on a circular cylinder in a uniform flow. *Phys. Fluids* **15**, 371–376.

Karniadakis, G. E. 1988 Numerical simulation of forced convection heat transfer from a cylinder in crossflow. *Intl J. Heat Mass Transfer* **31**, 107–118.

Karniadakis, G. E. & Triantafyllou, G. S. 1992 Three-dimensional dynamics and transition to turbulence in the wake of bluff objects. *J. Fluid Mech.* **238**, 1–30.

Kawaguti, M. & Jain, P. 1966 Numerical study of a viscous fluid flow past a circular cylinder. *J. Phys. Soc. Japan* **21**, 2055–2062.

Krall, K. M. & Eckert, E. R. G. 1973 Local heat transfer around a cylinder at low reynolds number. *J. Heat Transfer* **95**, 273–275.

Lange, C. F., Durst, F. & Breuer, M. 1998 Momentum and heat transfer from cylinders in laminar crossflow at $10^{-4} \leqslant \mathrm{re} \leqslant 200$. *Intl J. Heat Mass Transfer* **41** (22), 3409–3430.

Leonard, B. P. 1979 A stable and accurate convective modelling procedure based on quadratic upstream interpolation. *Comp. Meth. Appl. Mech. Engng* **19**, 59–98.

Mittal, R. 1996 Progress on les of flow past a circular cylinders. In *Annual Research Briefs*. Stanford, California: Center for Turbulence Research.

Mittal, R. & Balachandar, S. 1995 Effect of three-dimensionality on the lift and drag of nominally two-dimensional cylinders. *Phys. Fluids* **7**, 1841–1865.

Mittal, S. 2001 Computation of three-dimensional flows past circular cylinder of low aspect ratio. *Phys. Fluids* **13**, 177–191.

Nair, M. T. & Sengupta, T. K. 1996 Onset of asymmetry: flow past circular and elliptic cylinders. *Intl J. Num. Meth. Fluids* **23**, 1327–1345.

Nakamura, H. & Kamemoto, K. 2001 Numerical simulation of unsteady heat transfer around a circular cylinder to a uniform flow by a vortex and heat element method. *Trans. Japan Soc. Mech. Engng* B **67** (662), 137–144.

Norberg, C. 2003 Fluctuating lift on a circular cylinder: review and new measurements. *J. Fluids Struct.* **17**, 57–96.

Patel, V. A. 1976 Time-dependent solutions of the viscous incompressible flow past a circular cylinder by the method of series truncation. *Computers Fluids* **4**, 13–27.

Patnaik, B. S. V., Narayana, P. A. A. & Seetharamu, K. N. 1999 Numerical simulation of vortex shedding past a circular cylinder under the influence of buoyancy. *Intl J. Heat Mass Transfer* **42**, 3495–3507.

Patnaik, B. S. V. P., Seetharamu, K. N. & Narayana, P. A. A. 1996 Simulation of laminar confined flow past a circular cylinder with integral wake splitter involving heat transfer. *Intl J. Num. Meth. Heat Fluid Flow* **6** (4), 65–81.

Payne, R. B. 1958 Calculations of unsteady viscous flow past a circular cylinder. *J. Fluid Mech.* **4**, 81–86.

Persillon, H. & Braza, M. 1998 Physical analysis of the transition to turbulence in the wake of a circular cylinder by three-dimensional Navier-Stokes simulation. *J. Fluid Mech.* **365**, 23–88.

Pinol, S. & Grau, F. X. 1998 Influence of the no-slip boundary condition on the prediction of drag, lift, and heat transfer coefficients in the flow past a 2-d cylinder. *Num. Heat Transfer,* A: *Applics*. **34**, 313–330.

Sa, J. Y. & Chang, K. S. 1990 On the far-field stream function condition for two-dimensional incompressible flows. *J. Comp. Phys.* **91**, 398–412.

Schlichting, H. 1979 *Boundary-Layer Theory*, 7th edn. McGraw-Hill.

Schmidt, E. & Wenner, K. 1943 Heat transfer over the circumference of a heated cylinder in transverse flow. *Tech. Rep.* 1050. Nat. Advisory Cttee Aero.

Singh, S. P. & Mittal, S. 2003 Simulation of drag crisis in flow past a circular cylinder using 2D computations. *J. Aero. Sci. Tech.* **55**, 56–62.

Singh, S. P. & Mittal, S. 2004 Energy spectra of flow past a circular cylinder. *Intl J. Comput. Fluid Dyn.* **18**, 671–679.

Smith, P. A. & Stansby, P. K. 1988 Impulsively started flow around a circular cylinder by the vortex method. *J. Fluid Mech.* **194**, 45–77.

Son, J. S. & Hanratty, T. J. 1969 Numerical solution for the flow around a cylinder at reynolds numbers of 40, 200 and 500. *J. Fluid Mech.* **35**, 369–386.

Song, C. C. S. & Yuan, M. 1990 Simulation of vortex-shedding flow about a circular cylinder at high reynolds numbers. *Trans. ASME: J. Fluids Engng* **112**, 155–163.

Squire, H. B. 1938 Forced convection from a cylinder near the forward stagnation point. In *Modern Developments in Fluid Dynamics* (ed. S. Goldstein), pp. 631–632. Oxford University Press.

Sunden, B. 1983 Influence of buoyancy forces and thermal conductivity on flow field and heat transfer of circular cylinders at small reynolds number. *Intl J. Heat Mass Trans.* **26**, 1329–1338.

Ta Phouc Loc 1980 Numerical analysis of unsteady secondary vortices generated by an impulsively started circular cylinder. *J. Fluid Mech.* **100**, 111–128.

Ta Phouc Loc & Bouard, R. 1985 Numerical solution of the early stage of the unsteady viscous flow around a circular cylinder: a comparison with experimental visualization and measurements. *J. Fluid Mech.* **160**, 93–117.

Tezduyar, T. E. & Liou, J. 1991 On the downstream boundary conditions for the vorticity-stream function formulation of two-dimensional incompressible flows. *Comp. Meth. App. Mech. Engng.* **85**, 207–217.

Thom, A. 1933 The flow past circular cylinders at low speeds. *Proc. R. Soc. Lond.* A **141**, 651–669.

Thoman, D. C. & Szewczyk, A. A. 1969 Time-dependent viscous flow over a circular cylinder. *Phys. Fluids Supp.* II **12**, 76–86.

White, F. M. 1991 *Viscous Fluid Flow*, 2nd edn. McGraw-Hill.

Willden, R. J. & Graham, J. M. R. 2004 Multi-modal vortex-induced vibrations of a vertical riser pipe subject to a uniform current profile. *Eur. J. Mech.* B **23**, 209–218.

Williamson, C. H. K. 1996 Vortex dynamics in the cylinder wake. *Annu. Rev. Fluid Mech.* **28**, 477–539.

Wood, W. W. 1968 Calculations for anemometry with fine hot wires. *J. Fluid Mech.* **32**, 9–19.

Xia, M. & Karniadakis, G. E. 1997 Three-dimensional modeling of unsteady heat transfer. In *Proc. 1997 ASME Fluids Engineering Division Summer Meeting, Paper No. FEDSM97-3658, Part 7 of (of 24)*, pp. 1–6. ASME.

Zdravkovich, M. M. 1997 *Flow Around Circular Cylinders. Vol. 1: Fundamentals*. Oxford University Press.

Zdravkovich, M. M. 2003 *Flow Around Circular Cylinders. Vol. 2: Applications*. Oxford University Press.

Zhang, J. & Dalton, C. 1998 A three-dimensional simulation of a steady approach flow past a circular cylinder at low reynolds number. *Intl J. Num. Meth. Fluids* **26**, 1003–1022.

Zukauskas, A. & Ziugzda, J. 1986 *Heat Transfer of a Cylinder in Crossflow*. Hemisphere.